DEPARTMENT OF PHYSICS
UNIVERSITY OF JYVÄSKYLÄ
RESEARCH REPORT No. 9/2016

MODELING THE MECHANICAL BEHAVIOR OF CARBON NANOSTRUCTURES

BY
TOPI KORHONEN

Academic Dissertation
for the Degree of
Doctor of Philosophy

To be presented, by permission of the
Faculty of Mathematics and Natural Sciences
of the University of Jyväskylä,
for public examination in Auditorium KEM-1 of the
University of Jyväskylä on August 26th, 2016
at 12 o'clock noon

Jyväskylä, Finland
August 2016

Preface

The work presented in this thesis has been carried out during the years 2012-2016 at the Department of Physics and at the Nanoscience Center of the University of Jyväskylä. The work was supervised by Doc. Pekka Koskinen to whom I am grateful for guidance and support. We have had an easy-going journey where topics outside science have also been regularly discussed. I am also grateful to my collegues for creating relaxed and open minded working environment. It has been a joy to discuss various topics during the coffee and lunch breaks with you all. Special thanks to Robert van Leeuwen and all the current and former members of his research group for company also outside working hours.

I have been fortunate enough to end up in a band of extraordinary friends. You guys and gals have been laughing with/at me more than one could hope for. I am extremely grateful for your friendship, it has been a blast. I am also grateful to my parents and all the 'adults' who have guided me through my life. You have given me wings, literally. To both of my brothers I want to address special thanks, Ville for navigating me through unfamiliar cities, and Eetu for trying to inspire me into the world of organic shapes. Finally, I want to thank my girlfriend Essi for the wisdom and beauty that you bring into the lives of all the people around you.

Jyväskylä, August 2016

Topi Korhonen

Abstract

Low-dimensional nanostructures are expected to have vast number of applications in the future. Particularly large amount of research has been invested in the atom-thick carbon membrane called graphene, which has become popular due to its unique electronic and mechanical properties. This thesis presents studies of the mechanical and electromechanical properties of several different types of graphene nanostructures. In addition, short detours are performed in order to study the elasticity of gold nanostructures and topology effects in graphene nanoribbons.

The research is performed by using several different simulation methods. In simulations the system parameters and environment can be chosen at will, giving large amount of control over the studied phenomena. This control, and the access to different system parameters, can give insight into system properties that are hard to deduce from experiments alone. The reliability of the simulations depends on the used methods that are thus chosen according to the level of desired accuracy.

Large-scale deformations of graphene nanostructures are studied by classical force field methods. We present and explain edge rippling due to compression at graphene nanospiral perimeters when the nanospiral is elongated above a certain threshold. Further insight into the elastic behavior of these nanospirals is obtained by continuum elasticity modeling. For graphene nanoribbons we explain two previous experimental observations, an abrupt buckling under in-plane bending and the stability of curved graphene nanoribbon geometry on a smooth substrate. Buckling is predicted by simple model and is found to be due to the compression at the inner edge of the curved graphene nanoribbon. The stability of the curved geometry is shown to be due to registry effects between the graphene nanoribbon and the substrate. Moreover, intricate interlayer sliding patterns under peeling of multilayer graphene stacks are discussed and we show that such stacks are likely to recover after the peeling force is released.

Via electronic structure calculations we find a connection between the graphene nanospiral elongation and electronic structure and show that for graphene nanospirals the interlayer interactions play major part in the electronic structure near the structural equilibrium. Moreover, for graphene nanoribbons we study the effect of Möbius topology by using the revised periodic boundary conditions in a novel way. By the introduced method we are able to impose Möbius topology into flat graphene nanoribbons enabling the study of the role of the topology alone. We conclude that the topology affects only graphene nanoribbons with small length-to-width ratios. Finally we consider the temperature dependence of the bending rigidity of a two-dimensional gold nanostructure realizable in suitably sized graphene pores. The underlying motivation for most of the performed studies is the connection between the mechanical deformations and the electronic structure, which is discussed qualitatively even for large systems, where explicit electronic structure calculations are not possible.

Author's address Topi Korhonen
Department of Physics
University of Jyväskylä
Finland

Supervisors Adjunct professor Pekka Koskinen
Department of Physics
University of Jyväskylä
Finland

Reviewers Professor Tapio Rantala
Department of Physics
Tampere University of Technology
Finland

Associate Professor Jani Kotakoski
Faculty of Physics
University of Vienna
Austria

Opponent Professor Vivek Shenoy
Department of Materials Science and Engineering
University of Pennsylvania
United States of America

List of Publications

I T. Korhonen and P. Koskinen, *Electronic structure trends of Möbius graphene nanoribbons from minimal-cell simulations* Computational Materials Science **81**, 264-268 (2014).

II T. Korhonen and P. Koskinen, *Electromechanics of graphene spirals* AIP Advances, **4**, 12 (2014).

III T. Korhonen and P. Koskinen, *Peeling of multilayer graphene creates complex interlayer sliding patterns* Phys. Rev. B **92**, 115427 (2015).

IV T. Korhonen and P. Koskinen, *Limits of stability in supported graphene nanoribbons subject to bending* Phys. Rev. B **93**, 245405 (2016).

V P. Koskinen and T. Korhonen, *Plenty of motion at the bottom: atomically thin liquid gold membrane* Nanoscale **7**, 10140-10145 (2015).

The author has done all the numerical calculations and written the first drafts of articles [I, II, III, IV] excluding the calculation of the classical force field simulations of article [II]. The author has also implemented the continuum sheet elasticity code used in article [II] and programmed the constraint for atomistic simulation environment implementing the registry-dependent interlayer potential by Kolmogorov and Crespi used in articles [III] and [IV]. The author also programmed the first version of the routine for calculating the temperature dependence of the bending rigidity of two-dimensional gold nanostructures in article [V].

During his masters studies the author has also contributed in implementing the code for computing the components of self-energy presented in article:

- P. Myöhänen, R. Tuovinen, T. Korhonen, G. Stefanucci, and R. van Leeuwen, *Image charge dynamics in time-dependent quantum transport* Phys. Rev. B. **85**, 075105 (2012)

Contents

1 Introduction

The downscaling of silicon based electronics is not expected to continue further than the year 2026.[1] Considering the huge, and still increasing, importance of the information technology, it is clear that a material capable of replacing and outperforming silicon would be a great gift to the semiconductor industry. Graphene, the two-dimensional allotrope of carbon discovered in 2004,[2] is a material interesting even without technological considerations, but might also serve as a replacement for silicon. Graphene exhibits very large carrier mobility and field effect,[2] properties required from the silicon challenger, but it lacks an energy gap required by the conventional logic circuits. Without the energy gap devices fabricated from graphene always remain conductive and cannot be switched off effectively. An energy gap of ~ 1 eV is considered sufficient for logic applications, but despite numerous attempts such energy gap has not been achieved in graphene. However, one promising field at introducing energy gap in graphene is strain engineering, where by applying desired strain the electronic structure of graphene is modified opening interesting possibilities even if large enough energy gap is not achieved.[3, 4]

Strain engineering requires the knowledge of the electronic structure response to strain together with the understanding on how a given strain could be achieved by external stress. In addition, when we understand the effects of strains on the electronic structure, also the effects due to accidental strains in the graphene nanodevices can be predicted and the limits for acceptable deformations in a given application deduced. The knowledge of the electronic response to given strain is, however, useless without the knowledge how such strain can be achieved. This requires the study of the mechanical properties of graphene. These mechanical properties include extremely high in-plane stiffness together with very low bending rigidity, which make graphene sheets extremely flimsy and prone to ripple.[5, 6] The very existence of nonzero bending rigidity in a single atom thick membrane is in contrast to the mechanism suggested by the continuum sheet elasticity and thus the origin of the bending rigidity in graphene becomes interesting question in itself.

In this thesis we present results on the elastic behavior of graphene nanostructures. These results were obtained by various simulation methods including density-functional tight-binding, classical force fields, and continuum sheet elasticity methods. These studies were motivated by the possible control of the electronic properties via strain. However, though effort was given to relate the observed elastic deformation to the possible electronic structure modification, explicit electronic structure calculations were

only performed when allowed by the system size. The obtained results explain some experimentally observed phenomenon, as in our article [IV] for graphene buckling, or suggest not yet realized nanostructures and study their properties, as in our article [II] for graphene nanospirals. These results describe specific systems under specific constraints, but broader implications of the elastic and electromechanical behavior is considered by combining the results with other studies.

The thesis is constructed as follows. The methods are introduced in Chapter 2 where also some technicalities related to the numerical simulations are considered. In Chapter 3 selected results are introduced and further reviewed together with general introduction to the elastic properties of graphene. Chapter 4 summarizes the results and gives a brief outlook.

2 Simulation methods

2.1 Electronic structure simulations

In the description of the electronic conductance of a given solid the most common concept is the energy band structure of the solid. The band structure, continuum set of energy states in a given interval arises from the use of translational or other symmetries in the solid. The abuse of the symmetries are enabled by the Bloch's theorem which states that for any periodic potential the knowledge of wave function in one unit cell of the periodic system is sufficient in deducing the total wave function of the whole system. The band structure is then obtained by using the Bloch's theorem and solving the Schrödinger equation with the periodic potential produced by the nuclei which coordinates are given by the lattice structure. Particularly important feature of the band structure is whether there exists energy gap, *i.e.*, interval of energies that are not solutions to the Shrödinger equation, separating the conduction and valence bands. The size of the gap defines whether the material is metallic (no gap), semiconductor (small gap), or insulator (large gap). Graphene does not have energy gap, which makes its usage in conventional electronic circuits challenging. However, we can study the electronic structure response of graphene to various stresses and see if band gap can be created by such external manipulation.

According to quantum mechanics all available information of an interacting many-electron system is given by the wave function $\Psi(\boldsymbol{x}_1, \ldots, \boldsymbol{x}_N)$, where $\boldsymbol{x} = (\boldsymbol{r}, \sigma)$ are the position spin coordinates of the electrons. Using the Born-Oppenheimer approximation we treat the nuclear contributions as an external potential $V(\boldsymbol{x})$ for the electrons.[7] The stationary Schrödinger equation for the many-electron system in atomic units without external fields then becomes

$$\left[\sum_{i=1}^{N}\left(-\frac{\nabla_i^2}{2} + V(\boldsymbol{x}_i)\right) + \sum_{i<j} U(\boldsymbol{x}_i, \boldsymbol{x}_j)\right]\Psi_a(\boldsymbol{x}_1, \ldots, \boldsymbol{x}_N) = E_a\Psi_a(\boldsymbol{x}_1, \ldots, \boldsymbol{x}_N), \quad (2.1)$$

where $U(\boldsymbol{x}_i, \boldsymbol{x}_j)$ corresponds to the electron-electron interaction. In practise, for systems with more than a few electrons, this Schrödinger equation is impossible to solve even numerically since already the storage of the wave function in any decent space grid becomes impossible. Alternative approaches that reduce the amount of variables have thus been developed, including Green's function methods and density-functional theory. Our simulations, inaccessible with the more accurate methods, used density-

functional tight-binding and classical force field methods. Density-functional tight-binding is a quantum-mechanical method with approximations to reduce its computational cost, whereas classical force fields abandon the quantum-mechanical description altogether and describe the particle interactions via so-called classical potentials, which are a semi-empirical equations to describe the potential energy of a set of atoms with parameters fit to experimental results or quantum-mechanical simulations.

In this thesis electronic structure calculations were performed by the density-functional tight-binding method. Elasticity simulations with large amount of atoms under external stress were performed with classical force field simulations. Additionally some studies of the elasticity were performed by continuum sheet elasticity. The basic concepts of these methods are briefly introduced in the following.

2.2 Density-functional tight-binding method

Density-functional tight-binding (DFTB) is based on the density-functional theory (DFT). The starting point for DFT is the Hohenberg-Kohn (HK) theorem,[8] which states that for any two potentials $\hat{V} \neq \hat{V}' + C$ also the ground state wave functions $\Psi \neq \Psi'$. The HK theorem further shows that for non-degenerate ground states there exists a one-to-one correspondence between the ground state electron density and the external potential. This correspondence enables us to minimize the energy with respect to the density ($n(\boldsymbol{r}) = \langle\Psi|\hat{n}(\boldsymbol{r})|\Psi\rangle$) rather than with respect to the full wave function. All the observables in the ground state will be functionals of the density, and especially for the ground state energy we have

$$E_{\mathrm{gr}}[n] = \min_{n} F[n] + E_{\mathrm{ext}}[n], \tag{2.2}$$

where $F[n] = \langle\Psi|\hat{T} + \hat{W}|\Psi\rangle = T + E_{\mathrm{ee}}$ includes the total kinetic energy (T) and the electron-electron interaction energy (E_{ee}) and $E_{\mathrm{ext}}[n] = \langle\Psi|\hat{V}_{\mathrm{ext}}|\Psi\rangle = V_{\mathrm{ext}}$ includes the contribution due to the external potential (V_{ext}).

Usually also the Kohn-Sham system is introduced in order to separate the term $F[n]$ in Eq. (2.2) into pieces easier to approximate. The Kohn-Sham theorem [9] states that the ground state energy of a system can be calculated by solving the corresponding non-interacting Kohn-Sham system. The energy of the Kohn-Sham system is

$$E[n(\boldsymbol{r})] = T_{\mathrm{s}} + E_{\mathrm{ext}} + E_{\mathrm{H}} + E_{\mathrm{xc}}, \tag{2.3}$$

where we introduced Hartree energy term E_{H} due to the electron-electron Coulomb repulsion, kinetic energy of the non-interacting Kohn-Sham system T_{s}, and the exchange-correlation energy $E_{\mathrm{xc}} = T - T_{\mathrm{s}} + E_{\mathrm{ee}} - E_{\mathrm{H}}$ which hides all complicated many particle

effects. The Kohn-Sham orbitals ψ_a satisfy

$$\left(-\frac{1}{2}\nabla^2 + V_{\text{ext}}(\boldsymbol{r}) + V_{\text{xc}}[n](\boldsymbol{r}) + V_{\text{H}}[n](\boldsymbol{r})\right)\psi_a(\boldsymbol{r}) = \epsilon_a\psi_a(\boldsymbol{r}), \tag{2.4}$$

$$n(\boldsymbol{r}) = \sum_a f_a|\psi_a(\boldsymbol{r})|^2, \tag{2.5}$$

where f_a's are the occupation numbers, $V_{\text{H}}[n](\boldsymbol{r}) = \int n(\boldsymbol{r}')/|\boldsymbol{r}-\boldsymbol{r}'|\mathrm{d}^3r'$ is the mean field Hartree term, and $V_{\text{xc}}[n](\boldsymbol{r}) = \delta E_{\text{xc}}[n](\boldsymbol{r})/\delta n$ is the exchange-correlation potential. The total energy in Eq. (2.3) can be written with these Kohn-Sham orbitals as

$$\begin{aligned} E[n] &= \sum_a f_a \left\langle\psi_a\right| -\frac{1}{2}\nabla^2 + V_{\text{ext}} + V_{\text{H}}[n] \left|\psi_a\right\rangle \\ &- \frac{1}{2}\int V_{\text{H}}[n(\boldsymbol{r})]n(\boldsymbol{r})\ \mathrm{d}^3r + E_{\text{xc}}[n]. \end{aligned} \tag{2.6}$$

The task in DFT is to find proper approximations for the $E_{\text{xc}}[n]$ energy and then iteratively solve the Kohn-Sham Eqs. (2.4-2.6); after convergence both the ground state energy and density of the interacting system are known. This scheme has become extremely popular in many fields of computational chemistry and material physics.

To introduce the DFTB method we consider system with density n_0, which is a sum of densities of isolated atoms.[10] We assume that the actual density n minimizing Eq. (2.3) is close to n_0, *i.e.*, $n = n_0 + \delta n$, where δn is some small variation. We expand Eq. (2.6) to second order in δn, add ion-ion repulsion term E_{II}, rearrange, and obtain

$$\begin{aligned} E[n] &\approx \sum_a f_a \left\langle\Psi_a\right| -\frac{1}{2}\nabla^2 + V_{\text{ext}} + V_{\text{H}}[n_0] + V_{\text{xc}}[n_0] \left|\Psi_a\right\rangle \\ &- \frac{1}{2}\int V_{\text{H}}[n_0](\boldsymbol{r})n_0(\boldsymbol{r})\ \mathrm{d}^3r - \int V_{\text{xc}}[n_0](\boldsymbol{r})n_0(\boldsymbol{r})\ \mathrm{d}^3r + E_{\text{xc}}[n_0] + E_{\text{II}} \\ &+ \frac{1}{2}\int\int \left(\frac{\delta^2 E_{\text{xc}}[n_0](\boldsymbol{r})}{\delta n_0(\boldsymbol{r})\delta(\boldsymbol{r}')} + \frac{1}{|\boldsymbol{r}-\boldsymbol{r}'|}\right)\delta n_0(\boldsymbol{r})\delta n(\boldsymbol{r}')\ \mathrm{d}^3r'\mathrm{d}^3r. \end{aligned} \tag{2.7}$$

The second line in Eq. (2.7) is called the repulsive energy and it is approximated to depend only on the atomic distances

$$E_{\text{rep}} = \sum_{I<J} V_{\text{rep}}(R_{IJ}). \tag{2.8}$$

The pairwise repulsive functions $V_{\text{rep}}(R)$ are obtained by fitting to higher level DFT calculations.[10] The third line in Eq. (2.7) is due to charge fluctuations and it is here set to zero since charge transfer is expected to be small in our carbon systems. The first order terms in δn cancel out.

We assume that the core electrons are tightly bound to the core and thus they contribute mainly through the repulsive energy term in Eq. (2.8). We expand the $\psi_a(\boldsymbol{r})$ states with local minimal basis $\phi_\mu(\boldsymbol{r})$. These are eigenstates of a pseudo atom with an extra confining potential in order to mimic an atom in a solid. The expansion gives,

$$\psi_a(\boldsymbol{r}) = \sum_\mu c_\mu^a \phi_\mu(\boldsymbol{r} - \boldsymbol{R}_I), \tag{2.9}$$

where $\mu = (I, \mu')$ is double index running over all atoms I and their orbitals μ'. The approximate energy from Eq. (2.7) now becomes,

$$E[n] = \sum_a f_a \sum_{\mu\nu} c_\mu^{a*} c_\nu^a \langle \phi_\mu | \hat{H} | \phi_\nu \rangle + \sum_{I<J} V_{\text{rep}}(R_{IJ}), \tag{2.10}$$

where $\hat{H} = -\frac{1}{2}\nabla^2 + V_{\text{ext}} + V_{\text{H}}[n_0] + V_{\text{xc}}[n_0] \doteq -\frac{1}{2}\nabla^2 + V_{\text{s}}[n_0]$. Energy in Eq. (2.10) is minimized by variation $\delta(E[n] - \sum_k \epsilon_k \langle \psi_k | \psi_k \rangle) = 0$, where Lagrange multipliers ϵ_k are used to constrain the norms of $|\psi_k\rangle$ states. Variation gives a set of equations,

$$\sum_\nu c_\nu^a (H_{\mu\nu} - \epsilon_a S_{\mu\nu}) = 0, \quad \forall\ a, \mu \tag{2.11}$$

which can be viewed as a generalized eigenvalue equation with non-diagonal overlap matrix $S_{\mu\nu} = \langle \phi_\mu | \phi_\nu \rangle$. The Hamiltonian matrix elements $H_{\mu\nu} = \langle \phi_\mu | \hat{H} | \phi_\mu \rangle$ are approximated as

$$H_{\mu\nu} = \begin{cases} \epsilon_\mu, \text{ for } \mu = \nu \\ \langle \phi_\mu | -\frac{1}{2}\nabla^2 + V_{\text{s},I}[n_{0,I}] + V_{\text{s},J}[n_{0,J}] | \phi_\nu \rangle, \text{ for } I \neq J \\ 0, \text{ otherwise,} \end{cases} \tag{2.12}$$

where $V_{\text{s},I}[n_{0,I}]$ is the potential produced by the density of the free neutral atom I and similarly for J. Both the overlap and Hamiltonian matrix elements are calculated for a set of orientations and the rest of the elements are then obtained by the Slater-Koster transformation rules.[10] Solving Eq. (2.11) we obtain the eigenvectors c_μ^a that define the Kohn-Sham states $\psi_a(\boldsymbol{r})$ through Eq. (2.9) and ground state energy through Eq. (2.10).

For dynamics the forces on given atom can be calculated after Eq. (2.11) has been solved. Forces are gradients of the energy in Eq. (2.10) with respect to atomic positions $\boldsymbol{R}_I$,[10]

$$\boldsymbol{F}_I = -\frac{\partial E}{\partial \boldsymbol{R}_I} = \sum_a f_a \sum_{\mu\nu} c_\mu^{a*} c_\mu^a \left(\frac{\partial H_{\mu\nu}}{\partial \boldsymbol{R}_I} - \epsilon_a \frac{\partial S_{\mu\nu}}{\partial \boldsymbol{R}_I} \right) + \sum_{I<J} \frac{\partial V_{\text{rep}}(|\boldsymbol{R}_I - \boldsymbol{R}_J|)}{\partial \boldsymbol{R}_I}. \tag{2.13}$$

DFTB method is able to capture the interlayer interaction between graphene layers without additional terms introduced. However, the interlayer separation and the adhesion energy are not very accurately produced. Since the interlayer interaction given by DFTB method only played part in our article [II] which was more of a qualitative study we were satisfied with this description without the additional corrections.

2.3 Classical force fields

For the study of large systems or long time scales, inaccessible by DFTB, we used classical force fields. These methods omit the quantum-mechanical description by introducing classical potentials between particles. This reduces the computational cost significantly and enables simulations with several thousands or even millions of atoms. These potentials have large number of parameters that are fitted to higher level calculations and/or experiments to yield reasonable description of the desired systems.

Reactive empirical bond order (REBO) potential by Brenner,[11] based on the work of Abell [12] and Tersoff [13], is used to describe the interactions between carbon atoms. REBO potential uses only two body interactions, but incorporates the local environment of each atom into the description through terms depending on the number of neighbors of the given atom. Atom pair interacts with potential energy,

$$E_{ij}^{\mathrm{REBO}} = V_{ij}^{R}(r_{ij}) + \bar{b}_{ij} V_{ij}^{A}(r_{ij}), \tag{2.14}$$

where V^A is the attractive and V^R is the repulsive potential. The empirical bond order function $\bar{b}_{ij}$ incorporates the local environment of both atoms

$$\bar{b}_{ij} = \frac{1}{2}(b_{ij} + b_{ji}) + F(N_i, N_j, N_{conj}), \tag{2.15}$$

where $N_{i,j}$ is the total number of carbon and hydrogen neighbors of atoms i and j. The number N_{conj} depends on whether the bond between atoms i and j is part of a conjugated system. Each of these terms consists of several functions combined with hundreds of parameters that are fitted to known properties of hydrocarbons as described in Ref.[11].

The REBO potential produces many properties of hydrocarbon systems with good accuracy including the formation and breaking of covalent bonds. However, the range of REBO interaction is short and it does not describe the non-bonding interactions between the atoms. For multilayer graphene simulations we thus used separate interlayer potentials to describe the long range van der Waals interaction between the layers.

According to the level of description required two types of interlayer potentials were used. The popular Lennard-Jones potential [14] gives good adhesion description but considerably underestimates the energy differences related to the registry effects, *i.e.*, the lateral energy corrugations or the corrugation energy. The registry-dependent interlayer potential [15] gives reasonable description of both adhesion -and corrugation energies, though with increased computational demand.

Lennard-Jones interlayer potential

Lennard-Jones (LJ) potential [14] is widely used in computational chemistry due to its simplicity, as it only depends on the distance between the particles consisting of repulsive (r^{-12}) and attractive (r^{-6}) pieces. The attractive term represents the van der Waals interaction between atoms and has a long range. The repulsive term represents the Pauli repulsion due to the overlapping atomic orbitals when the atoms are brought closer together. Between two atoms the LJ-potential energy is given by

$$V_{\mathrm{LJ}}(r) = 4\epsilon \left[\left(\frac{\sigma}{r}\right)^{12} - \left(\frac{\sigma}{r}\right)^{6} \right], \tag{2.16}$$

where parameters ϵ and σ are given by best fit to higher level (DFT) calculations or experiments. For multilayer graphene we used values $\epsilon = 2.844$ meV and $\sigma = 3.4$ Å.[16] The potential is such that infinitely far apart the atoms have zero LJ-potential energy. For atoms approaching each other from infinity the LJ-potential energy is reduced until minimum is reached at distance $r_m = 2^{1/6}\sigma$ and energy $V_{\mathrm{LJ}}(r_m) = -\epsilon$. Decreasing the distance further from this rapidly increases the energy due to the repulsive term and the energy becomes zero again at $r = \sigma$.

The total LJ-potential energy for multilayer graphene is obtained by summing

$$E_{BT} = \sum_{\substack{i \in B \\ j \in T}} V_{\mathrm{LJ}}(|\boldsymbol{r}_i - \boldsymbol{r}_j|), \tag{2.17}$$

where B indicates the bottom and T the top layer. Further reduction of computational cost can be achieved if we assume that the bottom layer has a constant particle density n. Then an atom at height h above the bottom layer feels the LJ-potential that is roughly equivalent to integrating Eq. (2.16) with $r = \sqrt{R^2 + h^2}$ over the bottom layer $R \in [0, \infty[$. The result gives for an atom at height h LJ-potential energy

$$V_{\mathrm{LJ}}(h) = \frac{2}{5}\pi n \epsilon \left[2\frac{\sigma^{12}}{h^{10}} - 5\frac{\sigma^{6}}{h^{4}} \right], \tag{2.18}$$

where the particle density n for graphene is $n_{gr} = [3\sqrt{3}a^2/4]^{-1}$, and a is the bond distance between carbon atoms. However, the form in Eq. (2.18) can be used to describe also other substrates after choosing proper n, ϵ and σ.

Registry-dependent interlayer potential

Some of our simulations required accurate description of the lateral energy corrugations of the multilayer graphene. Due to the inability of the Lennard-Jones potential

to describe these lateral energy corrugations we used the registry-dependent interlayer potential by Kolmogorov and Crespi (KC).[15] The KC-potential gives fair description of the interlayer adhesion and lateral energy corrugations and was thus applied especially to simulations where interlayer sliding was present. The KC-energy between two atoms separated by $\boldsymbol{r}_{ij}$ is

$$V(\boldsymbol{r}_{ij}, \boldsymbol{n}_i, \boldsymbol{n}_j) = e^{-\lambda(r_{ij}-z_0)} \left[C + f(\rho_{ij}) + f(\rho_{ji})\right] - A \left(\frac{r_{ij}}{z_0}\right)^{-6}, \tag{2.19}$$

where functions $f(\rho)$ are taken to decay rapidly with transverse distance ρ,

$$\rho_{ij}^2 = r_{ij}^2 - (\boldsymbol{n}_i \cdot \boldsymbol{r}_{ij})^2, \tag{2.20}$$

$$f(\rho) = e^{-(\rho/\delta)^2} \sum_{n=0}^{2} C_{2n} (\rho/\delta)^{2n}, \tag{2.21}$$

and the surface normal $\boldsymbol{n}_i$ is normal to the sp^2 plane in the vicinity of atom i. The surface normals are calculated by normalizing the sum of the three normalized cross products between the displacements from atom i to its three nearest neighbors. We used the original parameterization, obtained by fitting to training set of experimental and theoretical results given in Ref. [15].

2.4 Revised periodic boundary conditions

For periodic lattices it is sufficient to apply the introduced DFTB description to the minimal unit cell of the system. This reduces the amount of simulated atoms tremendously. The ability to use periodicity of the lattice is due to the Bloch's theorem,[17] which states that for a translationally periodic system, $V(x) = V(x + L)$, with non-interacting electrons the knowledge of the wave function in one unit cell is sufficient for deducing the wave function of the whole system. However, Bloch's theorem can be further generalized to include general commuting symmetry operations.

Consider periodic potentials $V(\boldsymbol{r}) = V(\mathcal{S}^{\boldsymbol{n}}\boldsymbol{r})$, where $\mathcal{S}^{\boldsymbol{n}} = \mathcal{S}_1^{n_1} \ldots \mathcal{S}_k^{n_k}$ is a set of general commuting symmetry operations. It is possible to generalize Bloch's theorem to apply in systems with these potentials.[18, 19] Under general symmetry operation $\mathcal{S}^{\boldsymbol{n}}$ wave function $\psi_\kappa(\boldsymbol{r})$ attains merely a phase

$$\mathcal{D}(\mathcal{S}^{\boldsymbol{n}})\psi_{\boldsymbol{\kappa}}(\boldsymbol{r}) \doteq \psi_{\boldsymbol{\kappa}}(\mathcal{S}^{-\boldsymbol{n}}\boldsymbol{r}) = e^{-i\boldsymbol{\kappa}\cdot\boldsymbol{n}}\psi_{\boldsymbol{\kappa}}(\boldsymbol{r}), \tag{2.22}$$

where $\mathcal{D}(\mathcal{S}^{\boldsymbol{n}})$ is an operator defined by the first equal sign in Eq. (2.22) and $\boldsymbol{\kappa} = (\kappa_1, \ldots, \kappa_k)$ has now replaced the usual reciprocal space vector $\boldsymbol{k}$ and gets values either continuously or discretely depending on the boundary conditions of the corresponding

symmetry operation. If the underlying symmetry is genuinely periodic, as for example for the wedge symmetry, the κ_i sampling is discrete by the following consideration. Let N_i be the number of symmetry operations $\mathcal{S}_i$ after which the unit cell is mapped back to itself, then $e^{-i\kappa_i N_i} = 1 \Rightarrow \kappa_i = 2\pi m_i/N_i$, where $m_i = 0, \ldots, N_i - 1$. If the periodicity is not a genuine property of the system but a mere mathematical trick, as for example for translational symmetry, the corresponding κ_i can be divided into arbitrarily small intervals leading to the usual energy band description.

The Eq. (2.22) also implies, similarly to Bloch's theorem, that the wave functions in the periodic potential are of the form

$$\psi_{\boldsymbol{\kappa}}(\boldsymbol{r}) = e^{i\boldsymbol{\kappa}\cdot n(\boldsymbol{r})} u_{\boldsymbol{\kappa}}(\boldsymbol{r}), \tag{2.23}$$

where $n(\mathcal{S}^{-\boldsymbol{m}}\boldsymbol{r}) = n(\boldsymbol{r}) - \boldsymbol{m}$ and $u_{\boldsymbol{\kappa}}(\mathcal{S}^{-\boldsymbol{m}}\boldsymbol{r}) = u_{\boldsymbol{\kappa}}(\boldsymbol{r})$. The usage of general symmetry operations $\mathcal{S}$ gives in some cases substantial reduction in the computational effort. Similarly as the Bloch's theorem allows to consider the minimal translational unit cell, the Eq. (2.22) allows us to use general minimal unit cell that can greatly reduce the amount of atoms in the simulation cell, as for example in the case of chiral carbon nanotubes. Moreover, one can use these revised periodic boundary conditions at imposing non-trivial topologies to systems, as done in our article [I].

Chiral symmetry

In practise two symmetry operations, in addition to the translational symmetry, were used in the work presented in this thesis. The chiral symmetry describes the symmetry of a spiral curve, each section of angle $\Delta\phi$ is image of the minimal unit-cell with symmetry operation $\mathcal{S}^n = T_a^n R(\Delta\phi)^n$. Here, T_a is translation of length a along z-axis and $R(\Delta\phi)$ is rotation of $\Delta\phi$ around z-axis. The pitch of the spiral becomes $h = a2\pi/\Delta\phi$. If $\Delta\phi = 2\pi$, $\mathcal{S}$ reduces back to the translational symmetry operation. Additionally without the translation part the chiral symmetry reduces to the wedge symmetry, the second of the two used symmetry operations.

2.5 Structure optimization

Any configuration of atoms is associated with a potential energy due to the interactions between the atoms and the possible external potential. To optimize the lattice structure we want to find the configuration that minimizes the total energy of the system. Each atom has three space coordinates (spin excluded) and the problem is to minimize $E_p(x^1, y^1, z^1, \ldots, x^N, y^N, z^N)$ w.r.t. $3N \doteq M$ coordinates, where N is the number of atoms in the system.

Suppose function $f : \mathbb{R}^M \to \mathbb{R}$ is approximated around $\boldsymbol{x}_{n+1} = \boldsymbol{x}_n + \Delta\boldsymbol{x}$, where $\boldsymbol{x}_n = [x_n^1, y_n^1, z_n^1, \ldots x_n^N, y_n^N, z_n^N]^T$ and n denotes the iteration step, by Taylor series

$$\begin{aligned} f(\boldsymbol{x}_{n+1}) &\approx f(\boldsymbol{x}_n) + \sum_{i=1}^{M} \frac{\partial f}{\partial x^i}\Big|_{\boldsymbol{x}_n} \Delta x^i + \frac{1}{2}\sum_{i=1}^{M}\sum_{j=1}^{M} \frac{\partial^2 f}{\partial x^i \partial x^j}\Big|_{\boldsymbol{x}_n} \Delta x^i \Delta x^j, \\ &\doteq f(\boldsymbol{x}_n) + \Delta\boldsymbol{x}^T \boldsymbol{g}_n + \frac{1}{2}\Delta\boldsymbol{x}^T \boldsymbol{B}_n \Delta\boldsymbol{x} \doteq h_n(\Delta\boldsymbol{x}). \end{aligned} \tag{2.24}$$

Provided that the Hessian matrix $\boldsymbol{B}_n$ is positive definite, and we require it is, the minimum of the quadratic approximation can be evaluated by differentiating w.r.t. displacement $\Delta\boldsymbol{x}$,

$$\nabla h_n(\Delta\boldsymbol{x}) = \boldsymbol{g}_n + \boldsymbol{B}_n\Delta\boldsymbol{x} = 0 \Rightarrow \Delta\boldsymbol{x} = -\boldsymbol{B}_n^{-1}\boldsymbol{g}_n, \tag{2.25}$$

where the inverse $\boldsymbol{B}_n^{-1} \doteq \boldsymbol{H}_n$ is guaranteed to exist since the Hessian $\boldsymbol{B}_n$ was positive definite. The direction $-\boldsymbol{H}_n\boldsymbol{g}_n$ is taken for the displacement and $\boldsymbol{x}_{n+1} = \boldsymbol{x}_n - \alpha(\boldsymbol{H}_n\boldsymbol{g}_n)$, where the value of α is chosen to satisfy the Wolfe conditions,[20, 21] giving 'sufficient' decrease in the function value.

Due to the large computational demand in obtaining and inverting the Hessian matrix for systems with large number of coordinates approximations for the Hessian are used. The quasi-Newton methods approximate the Hessian at each step updating it based on the recent information of the objective function.[22] We already know that the Hessian is required to be symmetric $\boldsymbol{B} = \boldsymbol{B}^T$, however, we introduce another condition for the Hessian: the gradient of the approximation ∇h_{n+1} is required to be equal to the gradient of the function at the two latest iteration points, *i.e.*, $\nabla h_{n+1}(\Delta\boldsymbol{x})|_{\boldsymbol{x}_n} = \boldsymbol{g}_n = \nabla f(\boldsymbol{x}_n)$ and $\nabla h_{n+1}(\Delta\boldsymbol{x})|_{\boldsymbol{x}_{n+1}} = \boldsymbol{g}_{n+1} = \nabla f(\boldsymbol{x}_{n+1})$. This requirement is called as the secant condition. The latter equation is readily fulfilled by Eq. (2.25) since $\nabla h_{n+1}(0) = \boldsymbol{g}_{n+1}$. The former gives, again using Eq. (2.25), $\boldsymbol{B}_{n+1}(\boldsymbol{x}_n - \boldsymbol{x}_{n+1}) = \boldsymbol{g}_n - \boldsymbol{g}_{n+1}$ and we obtain for the inverse Hessian $\boldsymbol{H}_{n+1}$ a condition

$$\boldsymbol{H}_{n+1}\boldsymbol{y}_n = \boldsymbol{s}_n, \tag{2.26}$$

where $\boldsymbol{y}_n = \boldsymbol{g}_{n+1} - \boldsymbol{g}_n$ is the difference in the gradients and $\boldsymbol{s}_n = \boldsymbol{x}_{n+1} - \boldsymbol{x}_n$ is the difference in the coordinates. The Wolfe conditions for α guarantee the fulfilment of the curvature condition $\boldsymbol{s}_n^T\boldsymbol{y}_n > 0$ and consequently the existence of a solution for the secant equation Eq. (2.26).

BFGS-method

The quasi-Newton Broyden-Fletcher-Goldfarb-Shanno method (BFGS)[22] uses the secant condition together with the symmetry of the Hessian and approximates the evolution of the inverse of the Hessian matrix as a function of the differences $\boldsymbol{y}_n$ and

$\boldsymbol{s}_n$. However, infinite number of matrices satisfy the secant equation even with the requirement of symmetry, so to achieve unique $\boldsymbol{H}_{n+1}$ additional concept of closeness is introduced. The updated inverse Hessian $\boldsymbol{H}_{n+1}$ has to be close to the previous inverse Hessian $\boldsymbol{H}_n$ in terms of the weighted Frobenius norm,

$$\boldsymbol{H}_{n+1} = \arg\min_{\boldsymbol{H}} ||\boldsymbol{H} - \boldsymbol{H}_n||_{\boldsymbol{W}}, \tag{2.27}$$

where the weighting matrix $\boldsymbol{W}$ is the average Hessian.[22] The minimization is performed under symmetry- and secant conditions for the inverse Hessian. The result for the updated inverse Hessian matrix is

$$\boldsymbol{H}_{n+1} = \left(1 - \frac{\boldsymbol{s}_n \boldsymbol{y}_n^T}{\boldsymbol{y}_n^T \boldsymbol{s}_n}\right) \boldsymbol{H}_n \left(1 - \frac{\boldsymbol{y}_n \boldsymbol{s}_n^T}{\boldsymbol{y}_n^T \boldsymbol{s}_n}\right) + \frac{\boldsymbol{s}_n \boldsymbol{s}_n^T}{\boldsymbol{y}^T \boldsymbol{s}_n}. \tag{2.28}$$

This construction ensures that for positive definite $\boldsymbol{H}_n$ also the $\boldsymbol{H}_{n+1}$ will be positive definite. Then if the initial $\boldsymbol{H}_0$ is positive definite all successive Hessians shall also remain positive definite and Eq. (2.25) gives correct direction for the descent. The BFGS-method is effective in tackling large optimization problems if the initial guess is close to the actual solution. This is manifested by its popularity. BFGS was exclusively used for structure optimization in the studies presented. The convergence criteria was given by the maximum force an atom experiences in its position. If this force was smaller than 0.05 eV/Å for all atoms in the system the structure was considered to be relaxed.

2.6 Molecular dynamics

Molecular dynamics consists of numerically integrating equations of motion of the atoms in the system. The forces acting on each atom arise from the interactions between other atoms in the system and due to possible external potential. The equations for each atom are

$$m\frac{\mathrm{d}\boldsymbol{v}}{\mathrm{d}t} = -\nabla U(\boldsymbol{x}), \tag{2.29}$$

$$\boldsymbol{v} = \frac{\mathrm{d}\boldsymbol{x}}{\mathrm{d}t}, \tag{2.30}$$

where $\boldsymbol{x}$ is the position, $\boldsymbol{v}$ is the velocity, and m is the mass of the atom. Moreover, $U(\boldsymbol{x})$ is the potential due to other atoms and the possible contributions due to environment. The equations can be integrated for example by velocity verlet algorithm.[23] In practice the time step for integration is important; too large time step leads to inaccurate description while too small time step consumes unnecessary amount of computer time. We used time step of 2 fs for most of the simulations, however, for

cases where hydrogen atoms were compressed close to each other time step of 1 fs was required in order to achieve realistic dynamics.

When including the the effects of an environment on the system the simulation of the whole environment is often not feasible. For the description of a heat bath connected to the system we used Langevin dynamics.[24] This enables the thermalization of the studied system without a need for additional atoms in the simulation. The Langevin equation for each atom in the system reads

$$m\frac{\mathrm{d}^2\boldsymbol{x}}{\mathrm{d}t^2} = \boldsymbol{F} - \Gamma m\frac{\mathrm{d}\boldsymbol{x}}{\mathrm{d}t} + \boldsymbol{\eta}(t), \tag{2.31}$$

where $-\Gamma m\frac{\mathrm{d}\boldsymbol{x}}{\mathrm{d}t}$ is the friction due to the solution (environment), $\boldsymbol{F} = -\nabla U(\boldsymbol{x})$ is the force due to other atoms in the system and Γ is the damping parameter. The stochastic force $\boldsymbol{\eta}(t)$ is a Gaussian random force, due to kicks by environment particles, with probability distribution $p(\eta) = 1/\sqrt{2\pi}\sigma \times \exp(-\eta^2/(2\sigma^2))$, where $\sigma^2 = 2m\Gamma k_\mathrm{B}T$, where T is the temperature of the heat bath and k_B is the Boltzmann constant. The connection of the random kicks η and the friction via the damping parameter Γ guarantees that the system fulfills canonical ensemble statistics. The random kicks satisfy [24]

$$\left\langle \eta_i^\alpha(t)\eta_j^\beta(t')\right\rangle = 2m_i\Gamma k_\mathrm{B}T\delta_{\alpha\beta}\delta_{ij}\delta(t-t'), \tag{2.32}$$

where $\alpha, \beta \in \{x, y, z\}$ and i, j refer to different atoms in the system. There are no correlations of the random force neither in time nor in space.

The canonical ensemble averages can be approximated by time averaging [24]

$$\langle X\rangle = \left\langle \frac{1}{N}\sum_{l=1}^{N} X_l \right\rangle \approx \frac{1}{\tau_{ch}}\int_0^{\tau_{ch}} \left(\frac{1}{N}\sum_{l=1}^{N} X_l(t)\right)\mathrm{d}t. \tag{2.33}$$

Here the the damping time $1/\Gamma = \tau$, sets timescale for the dynamics. The characteristic times of the intrinsic dynamics τ_c, the times of molecular vibrations etc., need to be much smaller compared to the damping time $\tau_c << \tau$ in order to avoid overdamping. Moreover, the averaging time in Eq. (2.33) τ_{ch} needs to be much larger than τ in order to reach proper time averages. Usual value used for τ, in our classical force field (REBO) simulations was $\tau = 5$ ps.

2.7 Continuum linear elasticity

Let us now turn attention to the classical description of the continuum elasticity. Continuum implies that all considered length scales are large compared to the distances between atoms. Even the infinitesimal volume elements are expected to contain a large

number of atoms and the mathematical description of matter relies on continuous functions rather than discrete atomic positions. Even if the underlying assumptions are not fulfilled at nanoscale, the theory can be applied to graphene after introducing some minor modifications.

Whenever force is applied to a solid body a deformation occurs. The deformation is said to be elastic if the body recovers its initial shape and volume after the force is released. Elastic deformations are abundant in nature and for large systems well explained by the classical elasticity theory. Under the assumption of linear stress-strain relation the theory is called linear elasticity. Linear elasticity describes well deformations where the strains are small, although this does not necessarily imply that the deformation itself is small. The theory is rather complex even at the limit of small strains, but the derived equations for certain special cases, like uniform strain and uniaxial bending, are simple.

Solid bodies deform under external forces, *i.e.*, their shape, volume or both change. A position for a piece of material in the body is given by $\boldsymbol{r}$. Under deformation $\boldsymbol{r} \to \boldsymbol{r'} = \boldsymbol{r} + \boldsymbol{a}$ the distance between two nearby points ($\mathrm{d}l$) change according to

$$\mathrm{d}l'^2 = \mathrm{d}l^2 + 2u_{ij}\mathrm{d}x_i\mathrm{d}x_j, \tag{2.34}$$

where the strain tensor $\boldsymbol{u}$ is [25]

$$u_{ij} = \frac{1}{2}\left(\frac{\partial a_i}{\partial x_j} + \frac{\partial a_j}{\partial x_i} + \frac{\partial a_k}{\partial x_i}\frac{\partial a_k}{\partial x_j}\right), \tag{2.35}$$

and summation over repeated indices is implied.

The forces responsible for opposing the deformation and restoring the initial configuration are called internal stresses. Internal stresses arise from the molecular interactions and are short-ranged, extending only to the neighboring particles. The short-range of the molecular interactions lets us treat them as surface forces, provided each small volume $\mathrm{d}V$ contains sufficiently large number of atoms.[25] Force acting on a small surface $\mathrm{d}\boldsymbol{S}$ inside the body due to internal stresses is given by

$$\mathrm{d}F_i = \sigma_{ij}\mathrm{d}S_j, \tag{2.36}$$

where $\boldsymbol{\sigma}$ is the stress tensor. Using the conservation of the angular momentum, the stress tensor can be shown to be symmetric.[25] Without body forces each volume element inside the body experiences zero net force and the boundary conditions can be written

$$\frac{\partial \sigma_{ik}}{\partial x_k} = 0, \tag{2.37}$$

inside the body and

$$\sigma_{ik}n_k = P_i, \tag{2.38}$$

on the surface, where $\boldsymbol{P}$ is force per unit area and $\hat{\boldsymbol{n}}$ is the surface normal.

Assuming isotropic and homogeneous body we may expand the free energy density of the body in the strain tensor $\boldsymbol{u}$. In the equilibrium there should not be linear terms in $\boldsymbol{u}$. Moreover, there are only two independent scalars that can be formed from symmetric tensor of rank two. The expansion becomes [25]

$$\begin{aligned} F &= F_0 + \frac{1}{2}\lambda \mathrm{Tr}(\boldsymbol{u})^2 + \mu \mathrm{Tr}(\boldsymbol{u}^2) \\ &= \frac{1}{2}\sigma_{ij}u_{ij}, \end{aligned} \tag{2.39}$$

where λ and μ are the Lamé coefficients. On the second equality we used $\sigma_{ij} = \partial F/\partial u_{ij}$ and Euler's theorem $u_{ij}\partial F/\partial u_{ij} = 2F$.[25] Separating the strain tensor in components of pure shear and hydrostatic compression it can be shown that the stress and strain tensors are connected by

$$\sigma_{ij} = \frac{Y}{1+\nu}\left(u_{ij} + \frac{\nu}{1-2\nu}\delta_{ij}\mathrm{Tr}(\boldsymbol{u})\right), \tag{2.40}$$

$$u_{ij} = \frac{1}{Y}[(1+\nu)\sigma_{ij} - \nu\delta_{ij}\mathrm{Tr}(\boldsymbol{\sigma})], \tag{2.41}$$

where the coefficients

$$\begin{aligned} Y &= \frac{\mu(3\lambda+2\mu)}{2(\lambda+\mu)}, \\ \nu &= \frac{\lambda}{2(\lambda+\mu)}, \end{aligned} \tag{2.42}$$

are called Young's modulus (Y) and Poisson's ratio (ν).

Let us then calculate the effect of a longitudinal force acting on a rod parallel to $\hat{\boldsymbol{z}}$-axis. External forces are applied to the ends of the rod while the sides of the rod are free and Eq. (2.38) gives $\sigma_{ij}n_j = 0$ on the sides. Then, at the end of the rod, we must have all but $\sigma_{zz} \doteq p$ equal to zero. From Eq. (2.41) we obtain

$$u_{xx} = u_{yy} = -\nu\frac{p}{Y},\ u_{zz} = \frac{p}{Y}. \tag{2.43}$$

The meaning of coefficients Y and ν becomes clear. Young's modulus is the relation of the stress to the strain in the body. Poisson's ratio is the relation of the transverse compression to the longitudinal extension. The elastic energy density in Eq. (2.39) becomes

$$F = \frac{p^2}{2Y} = \frac{1}{2}Y\epsilon^2, \tag{2.44}$$

where in the last equality we denoted $u_{zz} \doteq \epsilon$ to recover the familiar form of the elastic energy density of uniform stretching. The free energy density in terms of Poisson ratio

and Young's modulus is

$$F = \frac{Y}{2(1+\nu)} \left\{ \mathrm{Tr}(\boldsymbol{u}^2) + \frac{\nu}{1-2\nu} \mathrm{Tr}(\boldsymbol{u})^2 \right\}. \tag{2.45}$$

Thin sheet elasticity

For thin sheets under small strains the forces required to bend the sheet are always much smaller than the internal stresses due to compression and extension of the parts of the sheet.[25] This lets us to set $P = 0$ in Eq. (2.38), giving $\sigma_{ij} n_j = 0$. For a sheet in $\hat{\boldsymbol{z}}$-plane we may conclude $\sigma_{iz} \approx 0$ for $i = x, y, z$. Since the sheet is thin and these components are small on both surfaces, we expect them to be small also between and thus negligible everywhere in the sheet. Then using Eq. (2.40) we obtain

$$\begin{aligned} \sigma_{xz} &= \frac{Y}{1+\nu} u_{xz}, \quad \sigma_{yz} = \frac{Y}{1+\nu} u_{yz} \\ \sigma_{zz} &= \frac{Y}{(1+\nu)(1-2\nu)} \left[(1-\nu) u_{zz} + \nu (u_{xx} + u_{yy}) \right]. \end{aligned} \tag{2.46}$$

Setting stresses in Eqs. (2.46) to zero and using the definition of strain tensor together with boundary condition $u_x(z=0) = u_y(z=0) = 0$, we obtain all the strain tensor components. The free energy density in Eq. (2.45) related to the small bending of a thin sheet becomes

$$F_b = \kappa_b \left\{ \frac{1}{2} \mathrm{Tr}(\boldsymbol{C})^2 + (1-\nu) \left[\mathrm{Tr}(\boldsymbol{C}^2) - \mathrm{Tr}(\boldsymbol{C})^2 \right] \right\}, \tag{2.47}$$

where $\kappa_b = h^3 Y / [12(1+\nu^2)]$ is the bending rigidity. We use the curvature tensor by do Carmo [26]

$$C_{ij} = \hat{\boldsymbol{n}} \cdot \frac{\partial^2 \boldsymbol{r}}{\partial x_i \partial x_j}, \tag{2.48}$$

where $\hat{\boldsymbol{n}}$ is the surface normal and x_i are the orthonormal coordinates of the tangent plane of the deformed sheet. The eigenvalues k_1 and k_2 of the curvature tensor C_{ij} form two invariants, the mean curvature $K = (k_1 + k_2)/2$ and the Gaussian curvature $K_G = k_1 k_2$.

When bending a flat sheet into a cylinder of radius R we get $k_1 = 1/R$ and $k_2 = 0$. The energy density becomes

$$F_b = \frac{1}{2} \kappa_b \left(\frac{1}{R} \right)^2. \tag{2.49}$$

Assuming small in-plane stretching and again setting Eqs. (2.46) to zero we obtain relations between components of the strain tensor $\boldsymbol{u}$. Using these relations and Eqs.

(2.40, 2.45) we obtain for the stretching energy density

$$F_s = \frac{\kappa_s}{1-\nu^2}\left\{\frac{1}{2}\left(u_{xx}+u_{yy}\right)^2 + (1-\nu)\left[u_{xx}u_{yy} - u_{xy}^2\right]\right\}, \tag{2.50}$$

where $\kappa_s = Yh$ is the in-plane stiffness for the sheet. Under uniform stretch $u_{xx} \doteq \epsilon$ the stretching energy in Eq. (2.50) becomes $1/2\kappa_s\epsilon^2$. We used the similar reasoning for the strain tensor components as before in Eq. (2.43). However, note that in the case of sheet the energy density is per surface area, not per volume as in Eq. (2.44).

The total energy density, stretching and bending, is obtained by integrating over the surface of the sheet

$$F = \int_S \left(F_s + F_b\right)\ \mathrm{d}S. \tag{2.51}$$

As mentioned, the continuum elasticity theory deals with systems of macroscopic length scales. It is particularly important to note how the bending rigidity and in-plane stiffness of thin sheets are connected via the Young's modulus and the thickness of the sheet. This is because the bending energy in Eq. (2.47) arises due to in-plane stresses around the neutral surface of the sheet. Being only single atom thick membrane graphene does not become under such in-plane stresses due to pure bending and the mechanism responsible for non-zero bending rigidity has to arise from different contributions. The modifications required are discussed in Ch. 3.2.

3 Mechanics and electromechanics of graphene nanostructures

3.1 Basic structure of graphene and graphene nanoribbons

Graphene is a single atom thick membrane of carbon atoms in a hexagonal arrangement with a bond distance of b =1.42 Å, Fig. 3.1.[27] The lattice structure is due to the hybridization of one s orbital with two p orbitals leading to a formation of strong σ bond. The remaining p orbitals perpendicular to the graphene plane bind covalently to the neighboring carbon atoms and form a half-filled π band that is responsible for the interesting electronic properties of graphene. The unit cell of graphene contains

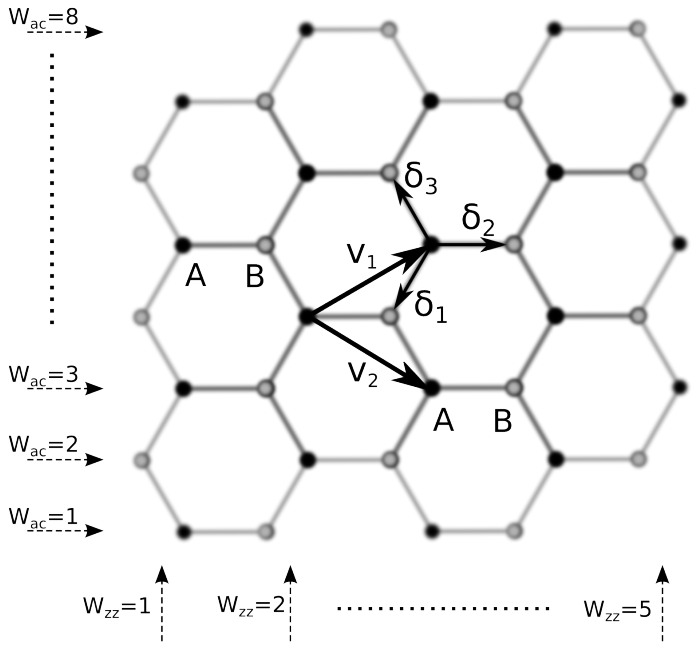

Figure 3.1: Graphene lattice and the two atoms in the unit cell A and B. The lattice vectors $v_{1,2}$ together with one of the nearest neighbor vectors $\delta_{1,2,3}$ define the hexagonal lattice. The arrows on the left denote the width convention for armchair (ac) graphene nanoribbons and the ones on the bottom denote the width convention for zigzag (zz) graphene nanoribbons.

two atoms, labeled A and B in Fig. 3.1. Energy bands derived from tight-binding Hamiltonian with only nearest neighbor hoppings included are [28]

$$E_{\pm}(\boldsymbol{k}) = \pm t\sqrt{3 + 2\cos\left(\sqrt{3}k_y b\right) + 4\cos\left(\frac{\sqrt{3}}{2}k_y b\right)\cos\left(\frac{3}{2}k_x b\right)}, \tag{3.1}$$

where $k_{x,y}$ are the components of the crystal momentum vector and $t(\approx 2.8$ eV [27]) is the nearest neighbor hopping energy. Near the Dirac points $\boldsymbol{K}$ and $\boldsymbol{K}'$ ($\boldsymbol{k} = \boldsymbol{K} + \boldsymbol{q},\ \boldsymbol{q} \ll \boldsymbol{K}$), at the corners of the first Brillouin zone, the energy bands in Eq. (3.1) reduce to

$$E_{\pm}(\boldsymbol{q}) \approx \pm\frac{3ta}{2}|\boldsymbol{q}| \doteq \pm v_f|\boldsymbol{q}|, \tag{3.2}$$

giving the famous linear dispersion relation between energy and momentum, resembling the energy spectrum of ultra-relativistic particles. Infinite graphene does not have an energy gap in this tight-binding description, and the zero energy gap of graphene is also supported by experiments.[2, 29, 30] If graphene is to replace silicon in electronic devices the introduction of an energy gap is crucial. Suggested methods for creating an energy gap include hydrogen absorption,[31] confining electrons by some external means,[32, 33] and strain.[4, 34–36] In this thesis the study of elastic properties of graphene systems is motivated by the possibility of controlling the electronic structure of graphene via strain.

For infinite graphene the zero gap feature is very robust against uniaxial strain. The gap opening is expected only for strains exceeding $\sim 20\%$.[34] It has even been shown that, in the tight-binding level, graphene should have zero gap at all reasonable uniaxial strains.[37] However, combined shear and uniaxial-strain could open energy gap of 0.9 eV at reasonable strains of $\sim 12\%$, highlighting the possibilities of complex strain patterns in graphene. [35] Indeed there are indications that non-uniform strains will lead to energy gap even in infinite graphene.[4, 38]

Graphene nanoribbons

In practise graphene samples come in various sizes and shapes. The size can vary tremendously, with dimensions ranging from very small, only few Angstroms wide ribbons, to very large industrial scale sheets. Small (< 100 nm) pieces with rectangular shape and high aspect ratio are called graphene nanoribbons (GNRs) and they are usually classified by the construction of their longer edge. GNRs with longer edge parallel to the ac-direction are labeled ac-GNRs and the GNRs with longer edge parallel to the zz-direction are labeled zz-GNRs (Fig. 3.1). The edges of these ribbons are typically hydrogen passivated, although other elements or functional groups are used as well. The edges can also be reconstructed with carbon rings of five or seven atoms.[39–41]

In ac-GNRs the lateral confinement of electrons creates energy gaps inversely proportional to ribbon widths,[32, 33] making them suitable candidates for electronics. Additionally, unlike in the infinite graphene, even small strain may affect ac-GNR's energy gap considerably.[42–45] The study of the elastic properties of the GNRs is thus motivated also from the electromechanical viewpoint.

3.2 Elastic properties of graphene and graphene nanoribbons

Being only single atomic layer thick, graphene is the thinnest possible membrane. Therefore the description of the elastic behavior of graphene using classical sheet elasticity is not straightforward, although possible, after the equations are modified in a proper manner. We introduce new elastic moduli and abandon the concept of thickness of the graphene monolayer. The modifications are due to the continuum assumption used in classical theory of thin sheet bending,[25] which in the case of monolayer graphene is illegitimate as there is neither compression nor stretching when bending a monolayer graphene with a zero Gaussian curvature.[46] However, with minor modifications the classical equations agree nicely with the simulations of graphene deformations.[47–50]

A general result states that hexagonal lattices are isotropic under in-plane stresses,[25] enabling the usage of single in-plane stiffness for graphene. The elastic moduli are obtained by fitting corresponding equations to simulations or, as in Ref. [5], by direct measurement. The bending rigidity κ_b becomes a module of its own, as there is no reason for it to be related to in-plane stiffness κ_s in the way derivation of Eq. (2.47) implies. The in-plane stiffness of graphene has been measured experimentally to be $\kappa_s = Yh = 340 \pm 50$ Nm^{-1}, which yields Young's modulus $Y = 1.0 \pm 0.1$ TPa with 'effective thickness' of 3.4 Å.[5] However, as already mentioned, there is no reason to consider thickness of graphene as it is used only to enable the usage of common classical elastic moduli like Young's modulus instead of in-plane stiffness. Moreover, the concept of effective thickness quickly leads to difficulties, if one tries to relate the bending rigidity to in-plane stiffness via the effective thickness.[51] The origin of these difficulties is the fact that graphene does not fulfill the assumptions used in the derivation of the classical sheet elasticity equations.[48, 52] Due to high in-plane stiffness and intrinsic strength, graphene is not only interesting due to its electronic properties, but it could also be used in futuristic applications requiring extreme strength, such as space elevators.[53]

Bending rigidity of graphene

Even when considering thin sheets, classical elasticity theory considers distances much larger than those between atoms. The bending rigidity follows from the in-plane extensions and compressions of the medium around the neutral surface.[25] This leads also to connection between the bending rigidity and Young's modulus. However, for graphene monolayer there is no need for the layer to neither compress nor stretch due to uniaxial bending since the graphene layer is its own neutral surface. The connection between bending rigidity and in-plane stiffness is then lost. The non-zero bending rigidity has to have a different origin compared to the classical sheets. Bond-order models have identified the origins of the bending rigidity to bond angle effects and to the bond-order term including dihedral angles,[51, 54] while considering bond orbital models the bending rigidity arises from a π-orbital misalignment between adjacent pairs of carbon atoms.[46] While the bending rigidity of a single atom thick membrane is interesting, in our simulations the bending rigidity showed only as an energy cost when graphene was bent; the mechanism responsible for this bending energy was not considered. The classical derivation of Eq. (2.47) also leads to relation between bending rigidity (κ_b) and Gaussian bending rigidity ($\bar{\kappa}_b$) which not necessarily applies for graphene. It is more safe to write Eq. (2.47) as [52]

$$F_b = \frac{1}{2}\kappa_b(k_1 + k_2)^2 - \bar{\kappa}_b k_1 k_2, \tag{3.3}$$

where $k_i = 1/R_i$ are the principal curvatures at given point and we have used the diagonal form of the curvature tensor $\boldsymbol{C}$ from Eq. (2.48).

We have now an equation for bending energy that was motivated from the classical description but has been modified to discard the consequences due to the continuum assumptions used in the derivation. For graphene we could have used the two invariants of the curvature tensor ($Tr(\boldsymbol{C})$ and $Tr(\boldsymbol{C}^2)$) and defined the bending energy density to be exactly the above Eq. (3.3) just by introducing the moduli κ_b and $\bar{\kappa}_b$ in a manner similar to the one used to introduce the original free energy in Eq. (2.39). After fitting the moduli κ_b and $\bar{\kappa}_b$ to simulations, Eq. (3.3) describes graphene bending with decent accuracy.[52]

Obtaining the bending rigidity for graphene is, by conventional simulations, a difficult task. Bending deformation breaks the translational symmetry, on which most of the programs implementing accurate (DFT) methods rely on.[46] Proper simulation thus requires relaxation of very large structures possible only by empirical potentials [55] or the consideration of graphene nanotubes and fullerenes.[6] However, the study of the bending rigidity and even the Gaussian bending rigidity become possible using the revised periodic boundary conditions and rotational symmetry.[56, 57] From DFTB method the obtained values are $\bar{\kappa}_b = -0.70$ eV and $\kappa_b = 1.61$ eV, which agrees roughly with the experimental value 1.2 eV determined from the phonon spectrum of

graphite.[58]

Graphene is, from inspection of the elastic moduli, extremely flimsy. Comparison with bilayer graphene shows tremendous difference in bending rigidity, $\kappa_b = 1.61$ eV for monolayer and $\kappa_b = 160$ eV for bilayer graphene, though there is large variation in the results for bending rigidity of bilayer graphene.[46] The large bending rigidity of the bilayer graphene is due to the inevitable stretching and compression in the graphene layers, regaining the sheet description, when bending with the layers clamped together from both ends. If not clamped, the layers in bilayer graphene may slide relative to each other and the bending rigidity is greatly reduced compared to the case that contains external clamps or sufficiently long tails that restrict the interlayer sliding. Due to the small bending rigidity single layer graphene easily ripples out-of-plane, as is manifested in a large number of results showing graphene rippling.[59–61] The rippling of graphene layer enhances its bending rigidity and is suggested to be responsible for the existence of free standing graphene in the first place.[62, 63] Understanding the elasticity of graphene is thus essential already in understanding graphene's very existence.

Temperature effects on bending rigidity

The temperature dependence of bending rigidity of graphene has been investigated finding both decreasing [64] and increasing [63, 65] bending rigidities when temperature is increased. For single layer graphene the increase in bending rigidity is attributed to the out-of-plane ripples due to thermal fluctuations.[63] These ripples are expected to increase the bending rigidity considerably, and indeed the measurements obtain much larger bending rigidities than the numerical predictions, for example Ref. [51] reported $\kappa_b \approx 7.1$ eV, several times larger than most of the computational estimates.

In addition to the carbon structures, the elasticity and bending rigidity of other types of materials was also studied. In our article [V] we used RPBCs to study the temperature dependence of the bending rigidity of two-dimensional gold membrane. Such membranes could possibly be realized in suitably sized pores made in graphene. Wedge unit cell containing 8×8 gold atoms was used together with rotational symmetry (Fig. 3.2a). While the article presented simulations predicting two-dimensional gold liquid at high temperatures in graphene pores, the bending simulation considered the bending rigidity of a two-dimensional gold in a solid phase. The RPBCs enabled such small unit cell that the DFTB method could be used in the simulation.

We simulated gold cylinders with radii 20, 30, 40, 50, 100 and 200 Å and fitted $1/R^2$ behavior, as suggested by Eq. (2.49), to the averaged (0.5 ns) energy differences ($\Delta E(R,T) = \kappa_b^{\mathrm{Au}}(T)/(2R^2) = E(R,T) - E_s - E(R=\infty,T)$) to obtain bending rigidity at different temperatures. The in-plane strain contribution (E_s) due to the

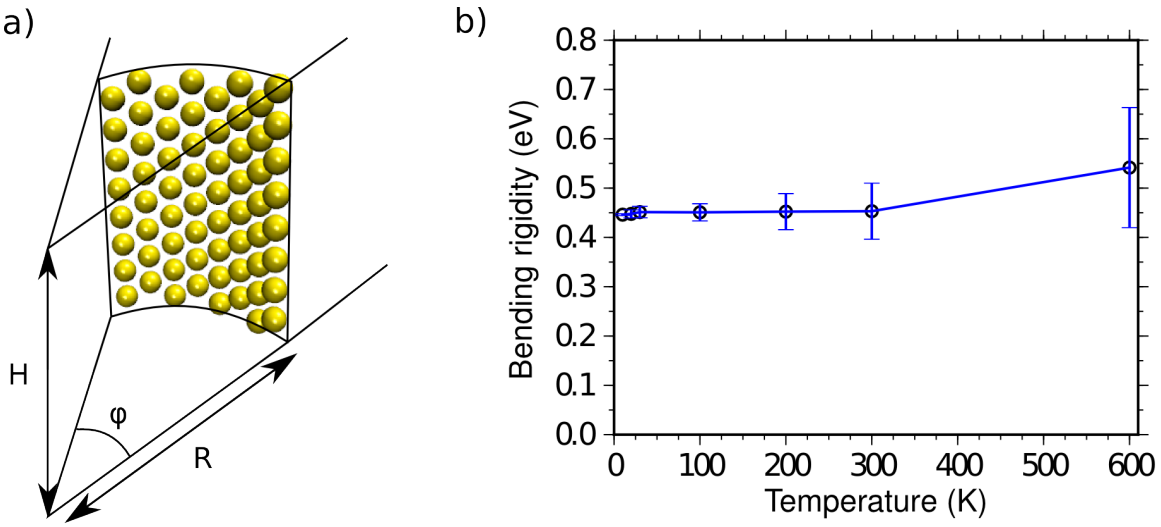

Figure 3.2: Simulations of the bending rigidity of two-dimensional gold. Left: Wedge unit cell and the 64 gold atoms. RPBCs with rotational symmetry was used in the simulations. Right: The bending rigidity of the two-dimensional gold surface increases slightly when temperature is increased.

radial wandering of the gold surface had to be subtracted from the averaged energy in order to obtain the energy due to the bending alone. We found a slight 0.3 meV/K rise in the bending rigidity as temperature was increased from 0 K to 600 K, though the standard deviation error bars arising from the fitting of the bending rigidity at each temperature are larger for higher temperatures (Fig. 3.2b). The results showed that for such gold membrane the bending rigidity was one third of the bending rigidity of graphene. The smaller bending rigidity of gold sheet may be due to the nature of the chemical bonding differences in gold and carbon. In graphene the carbon atoms bind covalently and these bonds are better at resisting bending compared to the less direction dependent metallic bonds in gold.

Edge stress in graphene nanoribbons

Description of the effects due to the graphene edges in GNRs requires an additional elastic energy term added to the classical sheet elasticity. This time we consider the in-plane stretching energy in Eq. (2.44). The construction of the GNR edges, where the uniform lattice ends, gives rise to an intrinsic edge stress. The edge stress magnitude and direction depend on the edge construction and can even lead to ripple formation at the edges if the edge stress is enhanced by functional groups.[66]

We model the edge stress by force τ ($[\tau] = \mathrm{eV/\AA}$) applied at the edges of the GNR. Except for the edges, where an edge in-plane stiffness is introduced, the ribbon maintains the in-plane stiffness of infinite graphene. The edge in-plane stiffness can be

included into effective in-plane stiffness $\kappa_s(w)$ and its effect especially in wider ribbons is small. The stretching energy density in Eq. (2.44) may be written for GNR with this additional edge stress as [67]

$$F_s = 2\tau\epsilon/w + \frac{1}{2}\kappa_s(w)\epsilon^2, \tag{3.4}$$

where w is the width of the nanoribbon. Edge stress τ can be evaluated once the reciprocal strain $\epsilon_c = -2\tau/(w\kappa_s(w))$ in the relaxed ribbon is known. This can be obtained from simulations by relaxing ribbons of length l_0 with given width and measuring the relaxed length l_c from which $\epsilon_c = l_c/l_0 - 1$.

We have now reviewed the general properties of graphene elasticity, discussed how and why the sheet elasticity is needed to be revised, and introduced the necessary concepts. We also discussed the motivation for the study of graphene elasticity through the strain engineering, as deformations in graphene could open possibilities to either enhance or modify the electronic properties of graphene in a controlled manner. Let us now focus on the articles presented in this thesis and give some additional details not emphasized in the article texts.

3.3 Topological Möbius graphene nanoribbons

Our article [I] introduced a peculiar way of imposing a Möbius topology on flat GNRs using non-trivial symmetries and boundary conditions. We called such ribbons topological Möbius GNRs (TMGNRs). Möbius ribbons, formed from strips by connecting the ends after giving one end a half-twist, are interesting objects in many aspects. For example, Möbius strips have only a single edge and a single surface so that traversing the ribbon length along the ribbon is equivalent to a π-rotation around the ribbon axis, *i.e.*, traversing the length of the ribbon twice is required in order to return to the starting point. The implications of this type of periodicity are interesting in contrast to the usual translational periodicity, where the Born-von Karman boundary conditions [68] connect the opposing sides of a bulk material. However, for a three-dimensional object in three-dimensional space this becomes impossible. For two-dimensional object the resulting topology is a torus and for one-dimensional object a ring. It is thus relevant to ask how much does the boundary conditions alone affect the system properties, since the actual systems in nature, apart from some special molecules, are rarely periodic in the fashion suggested by the Born-von Karman boundary conditions.

Recently Möbius topology was realized in experiments,[69, 70] and simulations of Möbius GNRs have been performed in Ref. [71]. However, our goal was not to consider genuine Möbius structures but to theoretically probe the effect of the Möbius topology alone. The structure of TMGNRs remained planar without any large deformations,

but the electronic wave functions satisfied the Möbius condition defined by

$$\mathcal{D}(T_{L_x})^M \phi^{\text{möb}}_{\kappa a} = \mathcal{D}(R_x)\phi^{\text{möb}}_{\kappa a}, \tag{3.5}$$

where T_{L_x} is a translation of L_x in $\hat{x}-$direction and R_x is a π rotation around x axis. The length of the ribbon becomes $L = ML_x$. We consider Hamiltonian invariant under translations T_{L_x} and π-rotations R_x, this implies that there should not be any direction-dependent terms in the Hamiltonian, *i.e.*, spin is excluded together with all vector fields not parallel with $\hat{x}-$direction. Provided these assumptions are satisfied, the Hamiltonian is also invariant under $S = T_{L_x}R_x \doteq TR$. We take this as the symmetry operation of our system. We can now show that the effect of the Möbius topology on the energy band structure of a GNR vanishes for long GNRs. Only ac-GNRs were considered due to possible spin polarization effects in zz-GNRs. Now for the symmetry operation S the periodic boundary conditions suggest

$$\mathcal{D}(TR)^M \phi_\kappa = \phi_\kappa \tag{3.6}$$

or

$$\mathcal{D}(T)^M \phi_\kappa = \mathcal{D}(R)^M \phi_\kappa = \begin{cases} \mathcal{D}(R)\phi_\kappa, & M = \text{odd} \\ \phi_\kappa, & M = \text{even}, \end{cases} \tag{3.7}$$

where we used $R^2 = 1$. We obtain Möbius topology for odd M and a ring topology for even M. Considering now the identical system with the usual Bloch's theorem, *i.e.*, with symmetry operation T, we get states

$$\begin{aligned} \mathcal{D}(T^n)\psi_k(\boldsymbol{r}) &= e^{-ikn}u_k(\boldsymbol{r}), & (3.8) \\ \Rightarrow \psi_k(\boldsymbol{r}) &= e^{ik\cdot x/L_x}u_k(\boldsymbol{r}), & (3.9) \end{aligned}$$

where $u_k(T\boldsymbol{r}) = u_k(\boldsymbol{r})$ and $k = 2\pi m/M$ with $m \in \{0, \ldots, M-1\}$.

Returning to the description with symmetry operation S we then separate the states into two classes, ϕ^+_κ that are even ($\mathcal{D}(R)\phi^+_\kappa = \phi^+_\kappa$) and ϕ^-_κ that are odd ($\mathcal{D}(R)\phi^-_\kappa = -\phi^-_\kappa$) under rotations R. For the odd states we have

$$\begin{aligned} \mathcal{D}(TR)^n\phi^-_\kappa(\boldsymbol{r}) &= \begin{cases} +\mathcal{D}(T)^n\phi^-_\kappa(\boldsymbol{r}), & n = \text{even} \\ -\mathcal{D}(T)^n\phi^-_\kappa(\boldsymbol{r}), & n = \text{odd} \end{cases} = e^{-i\pi n}\mathcal{D}(T)^n\phi^-_\kappa(\boldsymbol{r}) \\ &= e^{-i\kappa n}\phi^-_\kappa(\boldsymbol{r}), \\ \Rightarrow \mathcal{D}(T^n)\phi^-_\kappa(\boldsymbol{r}) &= e^{-i(\kappa-\pi)n}\phi^-_\kappa(\boldsymbol{r}), & (3.10) \end{aligned}$$

where on the second line we used Eq. (2.22). Comparing Eq. (3.10) with Eq. (3.8) and using boundary conditions $\kappa = 2\pi m/M$ with $m \in \{0, \ldots, M-1\}$, we deduce

$$\phi^-_k(\boldsymbol{r}) = e^{i(k-\pi)\cdot x/L_x}u_{k-\pi}(\boldsymbol{r}), \tag{3.11}$$

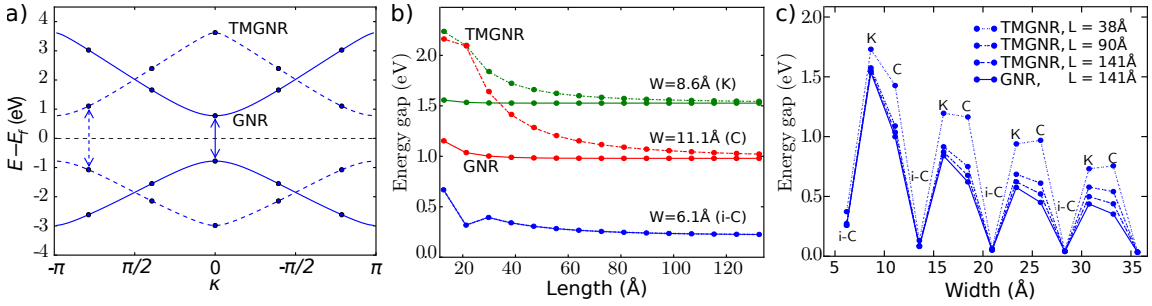

Figure 3.3: Energy band structure comparison between TMGNRs and GNRs and consequences in the energy gaps. a) Showcase of the band shift and the consequent energy gap change. The TMGNR's band (dashed line) is translated by $-\pi$ while the k-sampling remains identical. Only the highest occupied and lowest unoccupied bands are shown. b) Energy gap variation w.r.t. length for GNRs (solid lines) and TMGNRs (dashed lines) with three different widths. c) Energy gap variation w.r.t. width for GNR and TMGNRs with several lengths.

i.e., the odd states of the symmetry operation S are identical to the corresponding states of the symmetry operation T but they are translated in the k-space by $-\pi$. Similarly, the even states (ϕ_κ^+) of symmetry operation S become

$$\phi_k^+(\boldsymbol{r}) = e^{ik\cdot x/L_x} u_k(\boldsymbol{r}), \tag{3.12}$$

being identical to the even states of symmetry operation T. As suggested by Eq. (3.7) The Möbius topology was introduced by choosing M =odd.

For TMGNRs the energy bands corresponding to the odd states are translated by $-\pi$, but the k-sampling in both Möbius and ring topologies are identical, given by $k = 2\pi m/M$ with $m \in \{0, \ldots, M-1\}$. We now calculate the effect on the energy sum of occupied states in the odd bands due to the $-\pi$ translation of the odd bands. The energy of the odd states in Möbius ribbon is $E^{\text{möb}}(k) = E^{\text{straight}}(k-\pi)$, see Fig. 3.3a, then summing the energy of all the occupied odd states gives

$$E_{tot}^{\text{möb}} = \sum_{m=0}^{M-1} f_m E_T\left(\frac{2\pi m}{M} - \pi\right) = \begin{cases} \sum_{m=0}^{M-1} f_m E_T\left(\frac{2\pi m}{M}\right) = E_{tot}^{\text{straight}}, & M = \text{even}, \\ \sum_{m=0}^{M-1} f_m E_T\left(\frac{2\pi m}{M} + \frac{\pi}{M}\right) \neq E_{tot}^{\text{straight}}, & M = \text{odd}, \end{cases} \tag{3.13}$$

where f_m is the occupation number. To obtain the result we reordered the sums and used $E(k + 2\pi) = E(k)$. The band translation affects the total energy only for the TMGNRs (odd M). From Eq. (3.13) we observe that the energy difference between TMGNRs and GNRs vanishes as $M \to \infty$. In practise the energy difference became negligible already at small M corresponding to ribbon aspect ratios smaller than the smallest possible (~ 4 from Ref. [72]) for Möbius ribbons.

The band shift due to the topology had a subtle effect also on the energy gaps. If the bands responsible for the energy gap were both odd, they shifted due to the change in

the topology, whereas the k-sampling remained invariant. This gave raise to a possible change in the energy gap (Fig. 3.3a). This effect, which depended on the number of k-points, *i.e.*, on length of the ribbon, vanished quickly as M increased (Fig. 3.3b). The energy gaps of ac-GNRs and corresponding TMGNRs oscillated with width (Figs. 3.3c). For certain widths (i-C) the energy gap was due to even bands and remained almost unchanged upon changing topology. The minor energy gap change at short ribbons was due the relaxation of the TMGNRs to a slightly different geometries compared to GNRs.

The observed effects due to the topology were negligible for ribbons long enough to be twisted into Möbius configuration. Considering the energy contributions due to the topology alone (~ 0.05 meV/Å^2 for aspect ratios ~ 4) and comparing them with energy density even due to a small 1% strain gives immediately that the extra energy due the topology is negligible compared to the additional energy density anticipated from the strain effects. Simulations of the Möbius GNRs, with low aspect ratios, showed that these ribbons had large areas under considerable stress.[71] The stress patterns resembled those given by the classical sheet elasticity theory [72] and showed, as expected, that the elastic energy due to the strain is much larger than the energy increase due to the topology. In our setup we did not describe the finite Möbius ribbon structure and the strain contributions related to such structures were obviously lost. However, recalling the goal of the study, to examine the effects of the topology alone, we considered these restrictions of the method rather as an advantage. We concluded that the term 'k-point convergence' is not only with respect to the system size, but also with respect to the overall topology, *i.e.*, after certain size the system loses its perception of the topology and the boundary conditions lose their relevance.

3.4 Elasticity and electromechanics of graphene nanospirals

Nanodevices do not need to be flat, but they can also have complex three-dimensional structures or they can even be able to change form in a controlled manner.[62] One such structure could be graphene nanospiral, which can be viewed as a nano spring, at least if the interlayer interactions are excluded (Fig. 3.4b). In our article [II] we used DFTB and RPBCs to simulate the electromechanics and elastic properties of such graphene nanospirals as they were elongated. In addition, the elasticity of these nanospirals was considered by continuum sheet elasticity model. The suggested nanospirals could be surprisingly close to fabrication, as in Ref. [62] the authors already presented an experimental realization of one sort of a graphene nanospiral. The structure was still somewhat different from the ones we suggested, the radius of the nanospiral changed monotonically rather than stayed constant, but this was the first

experimental graphene nanospiral to our knowledge. Like Möbius GNRs, the nanospirals have a fascinating topology: partly one-dimensional (along the spiral axis), partly two-dimensional (radial and azimuthal dimension), and partly three-dimensional (interlayer interaction).

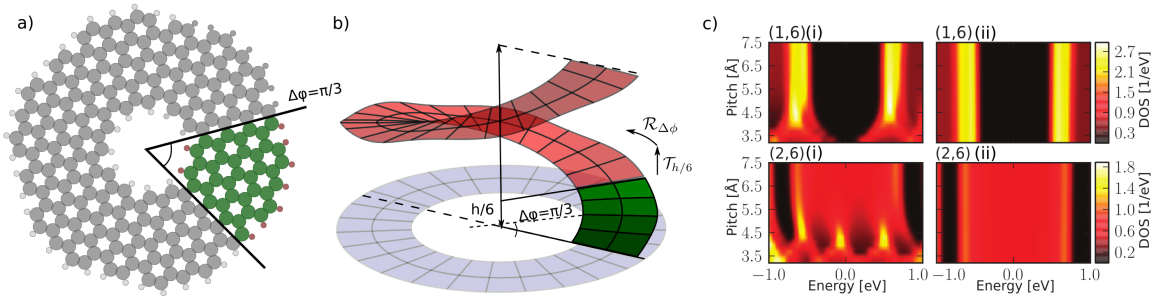

Figure 3.4: Graphene nanospiral simulations with DFTB and continuum sheet elasticity. a) Simulation setup, the atoms within the minimal unit cell are marked green. A wedge unit cell and chiral symmetry was used. b) The periodic images were obtained by rotating and translating the unit cell according to the picture. The pitch was fixed by the unit cell height. c) The density of states for two separate nanospirals under elongation with interlayer interactions turned on (left) and off (right). The changes near equilibrium pitch highlight the importance of the interlayer interactions. When the elongations were large the density of states were roughly equal as the interlayer interactions had lost their relevance.

The electronic structure simulations were performed by the DFTB method combined with the RPBCs in order to use the minimal unit cell (wedge with angle $\pi/3$) with the chiral symmetry (Fig. 3.4a,b). The elongation was controlled by the height of the unit cell which was varied slowly enough for the nanospiral to relax at each step. RPBCs allowed us to constrain the range of interactions to M nearest neighbor images of the unit cell. For $M < 7$ the interlayer interactions were effectively turned off, since the unit cell images on top of each other did not interact. This range M was independent of the κ sampling and gave only a limit for the interaction range in terms of symmetry operations rather than actual distance between the atoms. This setup was used to study the role of the interlayer interactions in the spiral.

We probed the changes in the electronic structure by considering the density of states near the Fermi level and showed that the electronic properties near the equilibrium pitch $h = 3.4$ Å are dominated by the interlayer interactions (Fig. 3.4c). When the interlayer interactions were included, elongating the nanospiral from the equilibrium pitch affected the density of states considerably. In contrast, when the interlayer interactions were not included the changes in the density of states only occurred at very large elongations when the in-plane strain became large. The relation between elongation and strain depends on the spiral geometry. In spirals with small inner radii elongations quickly start to stretch the bonds at the inner edge, making large elongations impossible. In contrast, spirals with large inner radii can withstand very large elongations, for some nanospirals elongations up to 2300% were simulated, cor-

responding to pitch of ∼78 Å(Fig. 3.4b).

The used symmetries and boundary conditions enabled the use of accurate DFTB method, but also introduced artificial constraints. The interlayer separation was forced to a constant of six times the unit cell height. Thus the periodicity made the elongation process take place uniformly throughout the nanospiral, whereas later, when considering finite-size nanospirals, we observed a local peeling process during the elongation. The structure of the nanospirals at small elongations was thus not likely well described by the simulations since constant interlayer spacing was not expected throughout the whole nanospiral. However, for large interlayer spacing, exceeding the effective range of the interlayer interaction, we expected the nanospiral structure to be well described by the periodic structure. Moreover, assuming a material with small van der Waals interlayer interaction compared to the bending rigidity, the layers could separate according to the periodic description as was seen in the case of the macroscopic spirals.

Elasticity of nanospirals

Under large elongations the deformations of the nanospirals showed unanticipated phenomena; after a threshold elongation a ripple quickly developed at the perimeter of the nanospiral (Fig. 3.5c and d). This rippling was only observed for a class of nanospirals with favorable geometry. In DFTB simulations the wavelength of this ripple was determined by the unit cell wedge angle and in order to understand the rippling more we developed a model based on the continuum sheet elasticity where also the wavelength of the ripple could vary. Our model neglected the edge stress contributions, but the constantly varying edge construction and the large deformations due to the elongation should justify this approximation.

The elastic model used continuum sheet elasticity combined with the chiral symmetry. Initially an annulus was cut in the radial direction into a wedge with an angle $\Delta\phi$ (Fig. 3.4a,b). The initial spiral structure was achieved with one end fixed and the other lifted to the desired height h_i resulting in a spiral with pitch $h = 2\pi h_i/\Delta\phi$. The elastic energy was then minimized by varying the nanospiral geometry while keeping the pitch constant. The geometry was controlled by five parameters that also allowed the ripple formation. Two boundary conditions were used to ensure uniform stretching along lines in azimuthal and radial directions within the spiral. We assumed the Gaussian bending rigidity in the bending energy term to be unimportant since changes in the Gaussian curvature always lead to stretching according to Gauss's *Theorema Egregium*;[73] this is extremely expensive due to the graphene's high in-plane stiffness.

The numerics were performed by calculating the components of the strain, in Eq. (2.35), and the curvature, in Eq. (2.48), tensors and minimizing the elastic energy in

Eq. (2.51) by varying the structure through the given parameters. We used the elastic moduli given by the DFTB method in order to be consistent with the atomistic simulations. The large amount of local minima in the parameter space led us to perform the energy minimization by the global optimization routine of basin hopping.[74] The elastic model captured the ripple formation in qualitative agreement with the DFTB simulations, *i.e.*, ripple formed in certain nanospirals after a threshold pitch was reached. With the insights given by the elastic model we were able to give qualitative reasoning behind the ripple formation.

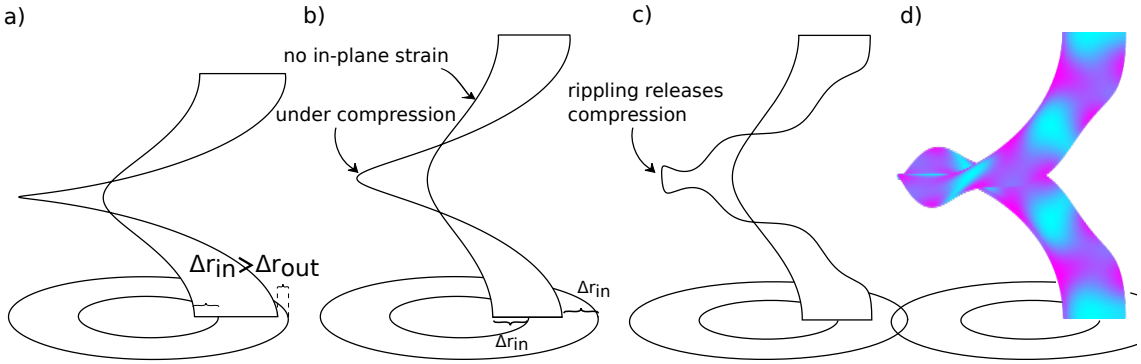

Figure 3.5: Rippling is a way to release excess compression from the spiral perimeter. a) Under elongation the spiral tends towards its axis. The required optimal shift depends on the radius and the inner and the outer edges prefer different shifts. b) The spiral shifts towards its axis avoiding stretch at the inner edge, but then the perimeter of the spiral becomes under compression. c) This compression can be relieved by rippling at the perimeter. d) Bending energy density shown on a nanospiral. Darker color corresponds to larger energy density and tighter bending.

The mechanism responsible for the rippling at the spiral perimeter is described in Figs. 3.5a, b, and c. Assuming no stretch for line arcs running in azimuthal direction along the annulus, we show that upon elongation into spiral the lines tend towards spiral axis as

$$r_i(h) = \sqrt{r_i^2 - \left(\frac{h}{2\pi}\right)^2}, \tag{3.14}$$

where r_i is the initial radius of the line arc and $r_i(h)$ is the radius of the spiral line with pitch h. The limit $h = 2\pi r_i$ corresponds to elongating an arc into a vertical line thus giving the ultimate limit for the no-stretch condition. Eq. (3.14) gives the required shift $\Delta r(r_i) = r_i - r_i(h)$ as function of the initial radius of the arc, being larger for smaller radii, see Fig. 3.5a for Δr_{in} and Δr_{out}. Elongation of an annulus into a spiral thus leads to stretch either in radial direction (widening of the annulus) or along the spiral curves (Δr is constant and spiral curves stretch and compress).

The high in-plane stiffness of graphene makes stretching and compressing suppressed whenever possible. Especially compression is in some cases easily relaxed if the graphene

can ripple out-of-plane. Due to the flimsiness of graphene, this rippling most often reduces the elastic energy since the reduction in the in-plane contribution is larger than the increase in the bending contribution of the total elastic energy. For the graphene nanospirals we found the structure with ripples to give minimal elastic energy. The formation of the ripples could be reasoned as follows. Consider a given annulus elongated into a nanospiral as described earlier. The nanospiral shifts according to the inner radius, *i.e.*, the line running at the inner edge remains at constant length during the elongation (Fig. 3.5a), whereas all the other lines in the nanospiral need to shorten (Fig. 3.5b). The shortened lines relieve the compression by rippling (Fig. 3.5c). The amount of compression, and consequently the amplitude of the ripple, increase with radius. In practice the processes were not this straightforward, the nanospiral did not shift only according to the inner radius, the widths of the nanospirals were small and there was only minor need for rippling. However, the underlying mechanism remained identical for all of the observed spirals that rippled during elongation.

Nanospirals with certain properties were more prone to ripple. The inner radius needed to be large enough to enable large elongations without considerable in-plane stretch. The nanospirals also needed to be wide enough ($w \sim r_i$) to ensure that the difference between the optimal shifts given by Eq. (3.14) at the inner and outer edges of the nanospiral were large enough for the compression to become considerable. To summarize, if the nanospiral was such that under elongation the perimeter came under sufficient compression, this compression was relieved by rippling. A formula for the compression at the perimeter, assuming above described process, of no-stretch at the inner edge, becomes

$$\epsilon_{r_i,w}(h) = \frac{\sqrt{r_i^2 + 2wr_i(h) + w^2}}{r_i + w} - 1, \tag{3.15}$$

where w is the nanospiral width. Eq. (3.15) has minimum, *i.e.*, maximum compression, at $w = r_i$ making spirals with width equal to the inner radius most prone to ripple.

Graphene rippling under compression was discussed already in the context of the edge stress in Ch. 3.2. However, here the rippling was caused by external elongation of the nanospiral, leading to compression at the perimeter in contrast to intrinsic edge stress of Ch. 3.2. Rippling due to excess compression is encountered again when discussing bending of GNRs on a substrate in Ch. 3.5. These types of rippling and buckling phenomena in graphene nanostructures can be expected in many forms due to the flimsiness of graphene. However, the predictions given by the classical sheet model encouraged us to perform a very crude experiment using spirals made out of plastic sheet and indeed the rippling was also observed in these macroscopic systems.

Classical force field modeling of the nanospiral elongation

Up to now we have only considered simulations performed for infinite nanospirals under specific symmetry operations and periodicities. This is due to the computational cost related to simulating large structures by the more accurate DFTB method. However, when studying the elasticity there was not as strong need for accurate quantum-mechanical methods as already apparent from the validity of the continuum sheet elasticity model. Classical molecular dynamics methods were thus used in the study of the elastic properties of finite sized nanospirals. These methods enabled good description of the elongation process while still allowing sufficient amount of carbon atoms to be simulated in order to study finite sized nanospirals.

We performed several simulations where graphene nanospirals with four full turns were elongated from the initial configuration with equilibrium layer spacing to a desired pitch. In contrast to the DFTB and the elastic simulations, where equidistant interlayer separation followed from the symmetry setups, in these finite systems the topmost layer of graphene peeled off locally. This local peeling was attributed to the strong van der Waals interaction between the graphene layers. Indeed, for large multilayered nanospirals it is not feasible to assume that the nanospiral should unfold with equidistant interlayer separations, since this would give very large energy cost due to the adhesion between the layers. The bending rigidity together with strength of the interlayer interaction define the mode of elongation of the nanospiral. With negligible interlayer adhesion and considerable bending rigidity the layers would peel with equidistant interlayer spacing. However, for the flimsy graphene with the sufficiently strong van der Waals interaction, the bending rigidity is not large enough to suppress the local peeling. The simulations showed how the peeling proceeded in local fashion as the nanospiral unfolded layer by layer. The local peeling was visible not only qualitatively in the simulations but also in the elongation force curve. The force remained roughly constant during the initial period of peeling when the force worked mainly against the adhesion between the layers. After the nanospiral had completely peeled, the force suddenly increased as in-plane deformations started to occur.

3.5 Bending of supported graphene nanoribbons

In our article [IV] we considered experiments by van der Lit *et al.* in Ref. [75], where 7-ac-GNRs were bent in-plane on an Au(111) substrate by an atomic force microscope tip at low temperature. The GNRs remained completely adhered to the substrate until a threshold curvature of ~ 4 deg/nm was reached and a part of the GNR buckled abruptly out of the substrate plane (Fig. 3.6a). Buckling relieved compression at the inner edges of the GNRs and allowed the GNR to attain new geometry with two

relaxed GNR pieces connected by the buckled region. The buckling curvature was denoted as a stability limit for bent GNRs on a substrate since before the buckling curvature the bending advanced smoothly in a uniform fashion whereas at the buckling curvature the whole geometry of the GNR suddenly changed. The experimental group also studied the maximum curvatures that could be maintained by the lateral energy corrugations, phenomenon called as pinning. We denoted also the maximal pinning curvature as a stability limit since under this curvature the GNRs could remain in pinned configuration, but above this curvature pinning was not observed.

We used classical force fields in a set of molecular dynamics simulations mimicking the experiments in Ref. [75] with the exception that, rather than pushing the outer edge of the GNR with a AFM tip, we twisted one end of the GNR while keeping the other end fixed. This way the deformation was better controlled and enabled simulation of shorter GNRs because the whole GNRs bent uniformly. In simulations twisting constraint was achieved by attaching an imaginary stick with heavy springs to the edge atoms at the free end of the GNR. This stick was then turned by a slow constant angular velocity while allowing it to move freely in the xy-plane (Fig. 3.6a).

The experiments were performed for GNRs on an Au(111) substrate.[75] In terms of simulation the gold substrate was not feasible due to the lack of a proper interlayer potential between graphene and gold. However, it turned out that the effect of the lateral energy corrugations should be negligible in the buckling simulations due to the bend geometry of the GNR and the high sensitivity of the corrugation energy to the GNR orientation.[76–78] When the GNRs were bent, large parts of them became out of registry with respect to the substrate below. Since registry effects in such situations are minor we chose interlayer potential describing only the adhesion between the GNR and the substrate, without any lateral structure. Therefore, in the buckling simulations, we used adhesion energy with the form suggested by the Lennard-Jones potential, given in Eq. (2.18).

The corrugation energy was not important for the description of the buckling process, but it was essential for the description of the pinning process. Pinning is due to a small piece of the GNR being in registry so that the bending moment due to the bend GNR is not sufficient in bringing this piece out of the registry due to the lateral energy corrugation barrier. Obviously for such a phenomenon the description of the corrugation energy was essential. Again, since no classical force field for graphene on a gold substrate was available, we departed from the experiment and made our simulations for GNRs on graphene. The KC-potential (Ch. 2.3,[15]) gives good description of the corrugation energy between graphene layers and was used in these simulations. We expected that in the end the precise form of the corrugation energy averages out and leaves only one effective parameter describing the strength of the lateral energy corrugations thus making the exact form of the substrate unimportant. The effective averaged parameter could then be fitted to describe also the experiments performed

on a gold substrate.

Bending-induced buckling

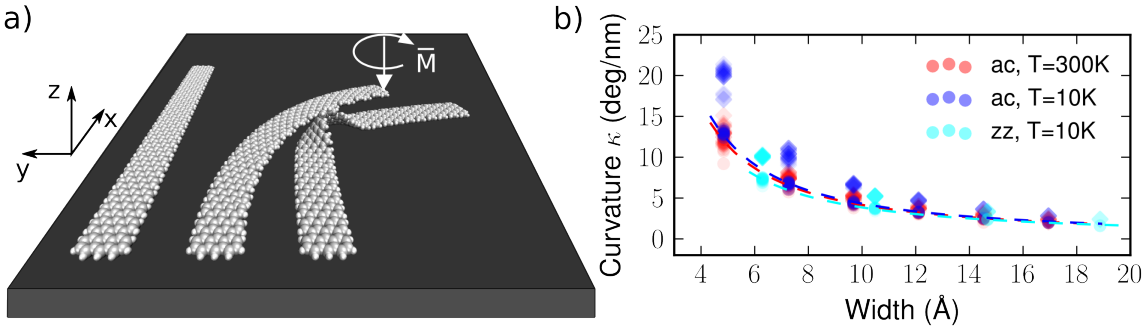

Figure 3.6: Buckling simulation setup and buckling curvatures for ac -and zz-GNRs. a) The simulation was carried out by twisting one end of a GNR by constant angular velocity while allowing it to move freely in the xy-plane. Buckling was observed as an abrupt out-of-plane deformation. After buckling the twisting direction was reversed and the simulation ended with the initial GNR geometry. b) Buckling curvatures given by the simulations. The larger curvature values (diamonds) correspond to the curvature for the formation of the buckle while lower values (circles) correspond to the curvature for the return to the flat configuration. Increased temperature reduced the hysteresis of the buckle formation and disappearance. Each of the simulations were repeated several times with different twisting rates.

Although the experiment used 7-ac-GNRs we considered several different ac-GNRs with widths 5, 7, 9, 11, and 13 as well as zz-GNRs with widths 4, 6, 8, and 10 (Fig. 3.1). The lengths of these GNRs were chosen such that the finite length effects due to the GNR ends were insignificant leading to width-to-length ratios of roughly 1/10. The simulations started by thermalizing the given GNR to 10 K and then twisting it until a major out-of-plane buckle was formed. The twisting was slow enough for the ribbon to deform uniformly. After the buckle formation the GNR was allowed to relax before the twisting direction was reversed. During the relaxation the two curved ends quickly recovered resulting two straight GNR sections connected by a buckled region (Fig. 3.6a). The GNRs remained buckled for some time even after the twisting direction was reversed, which resulted in a hysteresis loop for the buckling curvature. This hysteresis almost disappeared when temperature was increased to 300 K.

For ac-GNRs we observed rippling due to the compression at the inner edge as single ac-units started to point out of the GNR plane already at small curvatures well below the buckling curvature. Interestingly the wavelength (two ac-units) of this initial ripple remained constant until a large part of the GNR buckled (Fig. 3.6a). For zz-GNRs such rippling did not take place and the GNRs remained planar all the way to the buckling curvature.

Under uniaxial compression graphene is expected to buckle already at compressions of $0.5 - 1.5\%$ [79–83] However, in the described bending setup the compression at the inner edge was in many cases over 3% when the buckling finally occurred. In the bending setup buckling was suppressed by two factors: (i) out-of-plane buckling on a substrate decreased the adhesion energy [50] (ii) buckling would stretch the already stretched outer edge which increases the elastic stretching energy. Buckling only the inner edge, up to the neutral line of the GNR, is also suppressed due to the consequent change of the Gaussian curvature which implies stretching according to Gauss's *Theorema Egregium*.[73] Each of the possible ways of buckling thus lead to additional energy cost and hence the required compression for buckling was increased beyond the uniaxial compression limit. Fitting a simple model to buckling curvatures of ac-GNRs at 10 K temperature gave width dependent buckling curvature of

$$\kappa_b = \frac{360^\circ}{\pi}\left(\frac{0.0138\text{nm} + 0.023w}{w^2}\right), \tag{3.16}$$

which increases rapidly as $w \to 0$ (Fig. 3.6b). The model was fitted to the curvatures at which the buckles disappeared due to the random energy perturbations that help the experimental GNRs overcome any small energy barriers. This choice was further justified by the fact that the temperature decreased the buckling hysteresis and brought the buckle formation and disappearance curvatures close together. Unfortunately there are no experiments with varying GNR widths, so the prediction of buckling curvatures given by the simulations could not be verified yet. However, the value ~ 6 deg/Å for 7-ac-GNR agreed roughly with the experimental value ~ 4 deg/Å.

Pinning-enabled bending

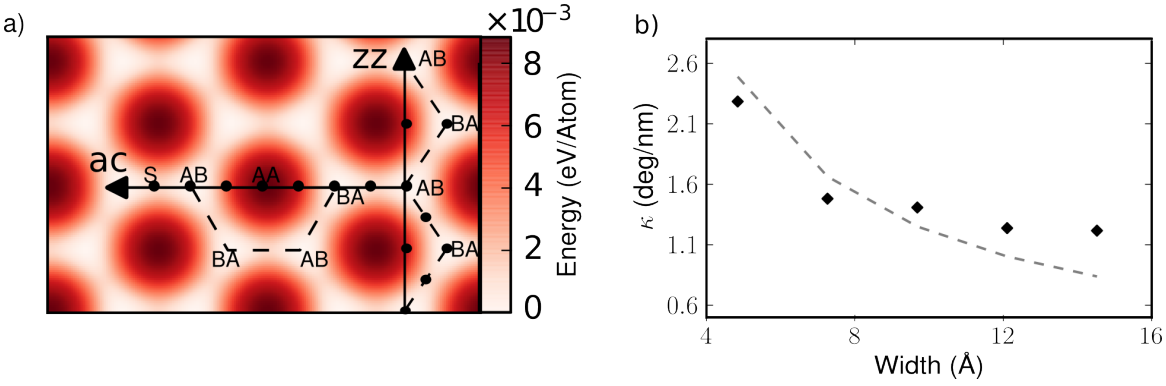

Figure 3.7: a) The lateral energy corrugation as given by the KC-potential between two aligned graphene layers. The dashed lines are the optimal sliding paths. b) The maximal curvatures possible with only the intrinsic tails of the bent GNRs. The dashed line gives prediction for the pinning curvature from the simple model.

In our simulations of the pinning process we considered GNRs on a graphene substrate since this enabled us to describe the interlayer interactions by the KC-potential. Even if our choice of substrate departed from the experiment, we expected it to give insight into the GNR pinning phenomenon in general. The corrugation energy for oriented graphene layers given by the KC-potential is shown in Fig. 3.7a. If the layers are rotated the energy differences between different lateral positions reduce and the potential soon loses its lateral dependence as was already assumed in the buckling simulations and as is also shown by experiments.[76–78] However, for us the discussion of the corrugation energy between non-oriented layers is rather unimportant as in practise smaller flakes tend to slide into registry [84] and larger flakes may get distorted in order to obtain the registry.

Experiment in Ref. [75] presented phenomena where 7-ac-GNRs remained in bent configurations ($\sim$ 2 deg/nm) even without any visible constraints. These stable curves were attributed to the lateral energy corrugations between the GNR and the gold substrate. Our simulations showed that GNRs could be held in such curved configurations if even a small piece of GNR was set in registry with the substrate. When the force keeping the pinned piece in registry was larger than the force due to the bend GNR the whole GNR remained pinned into the curved geometry.

In our simulations a bent GNR (optimized circular arc of angle $\pi/3$) was set on a graphene substrate with one end in-registry and the other end fixed by an external constraint. Additional tail of in-registry straight GNR was added to the free end and the resulting GNR was let to thermalize and relax. Usual time scale for sliding off from the registry was few ps at temperature of 10 K, leaving plenty of relaxation time for the pinned GNRs that were required to remain in initial registry for 20 ps. However, when the temperature was increased the GNRs could be brought out of registry even after considerable simulation times ($\sim$15 ps). We expected the increase to be due to the temperature fluctuations, but proper understanding of the dynamics would have required simulation times beyond our computational reach.

Longer added tails were able to maintain curves with smaller radii. However, even without the additional tail there was always a short piece of GNR close to registry at the free end of the GNR. This piece, the 'intrinsic tail', was also sufficient in maintaining the GNR in the bent configuration, provided the curvature radius was large enough, see Fig. 3.7b. The intrinsic tail was sufficient at pinning GNRs with edge compression from $\sim$ 0.9 % for N = 5 to $\sim$ 1.5 % for N = 13. The width dependence might be due to thermal fluctuations, which affect narrow GNRs more due to fewer amount of pinned atoms.

In experiments the GNRs were bent into the pinned configurations intentionally, but similar deformations of the GNRs can, to some extent, be expected even without deliberate modifications. The electronic properties of the GNRs can be modified by

in-plane bending [85] and it is thus important to understand the amount of curvature that could, in principle even accidentally, be realized on a smooth surface because of the pinning. Here, we probed some limits for such deformations. Although, it is unlikely that GNRs would attain the tightest of the curvatures maintained by pinning without intentional modifications, even smaller curvatures can change the electronic properties of the GNRs and modify the system properties.

3.6 Peeling of multilayer graphene stacks

In our article [III] we simulated peeling of multilayer graphene stacks by external force at 10 K temperature (Fig. 3.8). The simulation mimicked the experimental setup of Ref. [86], where molybdenum disulphide stacks of selected thicknesses were peeled by an AFM tip. The results indicated preferred angles where the required peeling force suddenly decreased. In addition, thick enough stacks were found to remain in the kinked geometry at certain preferred angles, even after the external peeling force was released. These experimental results motivated the study of similar peeling phenomenon in multilayer graphene stacks.

As mentioned the bending rigidity of multilayer graphene is greatly enhanced when increasing the layer number. This is due to the connection between bending and in-plane stress if these layers are clamped together at the ends. However, in our simulation setup the graphene layers were not clamped together and due to the small interlayer shear resistance they slid relative to each other rather than deformed in-plane. The behavior of the multilayer graphene stack under peeling and the concomitant bending was largely dominated by the interlayer interaction. We studied the resulting sliding patterns and observed that the layers slid along staggered paths avoiding the low adhesion energy of the AA-stacking. These relative paths followed the optimal paths presented in Fig. 3.7a. Indeed, the resulting microscopic dynamics, interlayer shear patterns perpendicular to the peeling direction, were not explained by linear sheet elasticity, but required considering the lateral energy corrugations before they could be understood. We further showed that due to the rather low barriers in the corrugation energy, these multilayer graphene stacks are always likely to recover after a peeling force is released. This differs from the molybdenum disulphide stacks that were observed to remain in the kinked configurations most likely due to the corrugation energy effects.[86]

Detailed discussion of the simulation procedure is given in our article [III]. Here the sliding patterns and kinking mechanism are discussed in more detail. KC-potential (Ch. 2.3, [15]) was used and the resulting corrugation energy (Fig. 3.7a) was important in explaining both the sliding patterns and the kinking mechanism. In the following discussion I shall use the coordinates given in Fig. 3.8, the peeling direction is $-\hat{x}$

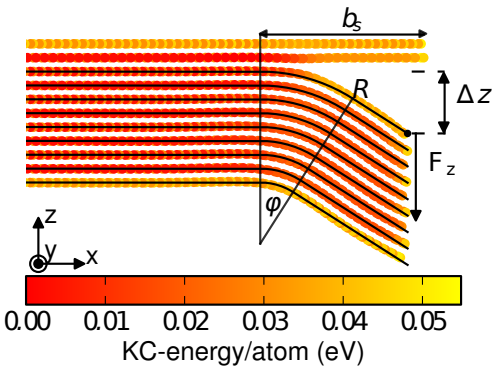

Figure 3.8: Peeling setup used in the simulations. The rightmost atoms of the topmost layer of the peeled stack were pulled down with a small constant velocity resulting in quasistatic dynamics. The pulled atoms were allowed to move freely in the xy plane. Layer curves in xz-plane were approximated by two lines connected by circular arcs, in total three fitting parameters were used for all of the layers. The radii of the arcs were defined from the constant interlayer distance and from the radius of the topmost layer. The system was periodic in the $\hat{y}$-direction and long enough for the fix at the left end to be irrelevant.

which is also, when discussing interlayer sliding, taken as the sliding direction of the layers even though the real layer sliding direction is in the xz-plane.

Pinning multilayer graphene to kinked configuration is unlikely

After the peeling and concomitant bending started the graphene layers began to slide relative to each other (Fig. 3.8). The stacking of multilayer graphene is unaffected by shift of any individual layer by integer multiple of the graphene lattice vectors (Fig. 3.1). Since the layers slid relative to each other there was a possibility to bend the multilayer stack in a manner where the areas around the bend were in registry, *i.e.*, the registry was lost only at the bend region. The simple idea presented already in Ref. [86] assumes that the layers neither stretch nor compress but only bend and slide. Consider N-layer graphene stack peeled as in Fig. 3.8, the layers atop slide in $-x$-direction w.r.t. layers below. Given a simplistic description of the system, we approximate each layer as two straight lines connected by a circular arc of angle ϕ and radius $R_i = R - h \cdot i$, where $i = 0, \ldots, N-1$. In this model neighboring layers get a relative shift

$$\Delta l = h\phi, \tag{3.17}$$

where h is the interlayer separation. Relation between the period of the corrugation potential (a) and the interlayer separation define the optimal angle ϕ_r for which the layer shifts $\Delta l = a$ and the stacks around the bend region are in registry. The period of the corrugation potential depends on the peeling direction being $a^{\mathrm{ac}} = 3b$ (b is the bond distance) in ac-direction and $a^{\mathrm{zz}} = \sqrt{3}b$ in zz-direction. These give optimal angles of $\phi_r^{\mathrm{ac}} \approx 72°$ and $\phi_r^{\mathrm{zz}} \approx 41°$. In the simulations only the optimal angle ϕ_r^{zz} for

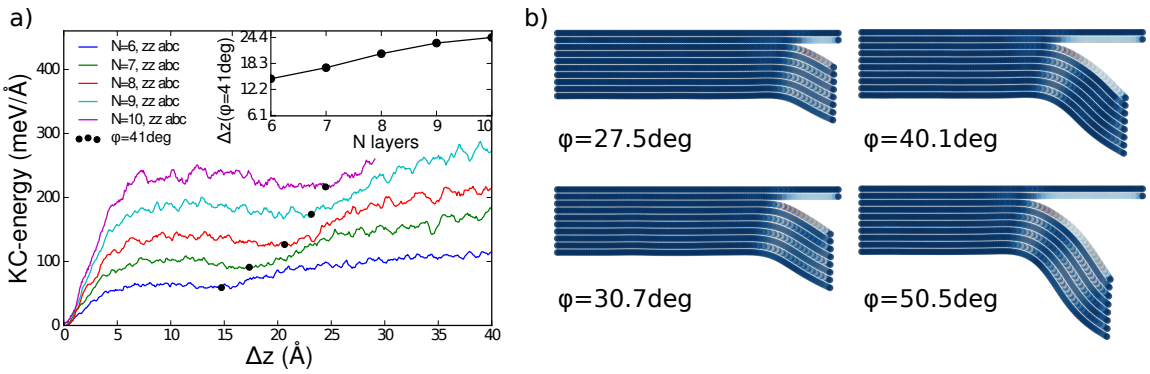

Figure 3.9: KC-energy when peeling in zz-direction. a) KC-energy as a function of the pulling distance Δz (Fig. 3.8). A minimum was observed roughly at the position of the optimal bend angle ϕ_r. Inset: The required pulling distance for optimal bend angle $\Delta z_N(\phi_r)$. b) Snapshots of the structure under peeling with KC-energy difference between initial and peeled configurations shown by color (dark blue = no change, light = some change, red = major change). Close to optimal angle $\phi_r^{\rm zz}$ (right up corner) the bulk part after the bend region attained good registry and minimized the KC-energy as visible by the dark blue color.

peeling in zz-direction was reached. However, when peeling in the ac-direction it was possible to obtain optimal stackings, even if the shift did not match the full period of the corrugation potential. The required shifts depended on the initial stacking, but with shifts of $a^{\rm ac} = b$ or $a^{\rm ac} = 2b$ transitions from AB- to BA-stacking or vice versa were achieved (Fig. 3.7a) and registry in the corresponding cases obtained.

In Fig. 3.9a we plot the recorded KC-energy for peeling in the zz-direction. The KC-energy has local minimum roughly at pulling distances Δz corresponding to the optimal $\phi_r^{\rm zz} = 41°$ angle. This minimum, should it have been deeper, could have locked the stack in the kinked geometry as was observed in the experiments for molybdenium disulphide. However, the stack always recovered the initial flat geometry after the peeling force was released and the registry effects seemed unable to lock the multilayer graphene stack into a kinked geometry. In order to highlight the registry change in the peeled part when approaching the optimal angle we show the difference in the KC-energy of individual atoms w.r.t. the peeling angle in Fig. 3.9b. The peeled part obtains almost perfect registry near the optimal angle as visible from the color change from bright to dark.

Bending by an angle ϕ_r and the concomitant interlayer slides as presented here gives possibility to modify the stacking of a multilayer graphene. Consider initially ABC stacked graphene. Now bend it along zz-direction by $\sim 25°$ which corresponds to sliding in the corrugation potential from AB -to BA-stacking (Fig. 3.7a). The stacking after the bend changes into CBA. Making another bend returns the stacking back to ABC. Multilayer graphene constructed by alternating the bend direction, and consequently stacking (Fig. 3.10), could posses interesting electronic properties since

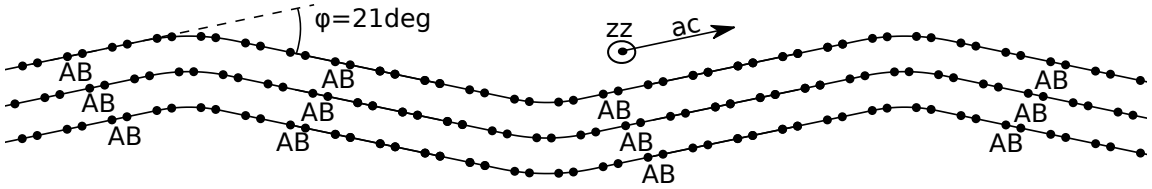

Figure 3.10: Alternating stacking in multilayer graphene achieved by staggered bending in zz-direction. The dots represent carbon atoms of single ac-line.

stacking can change the electronic properties considerably along the structure.[27] However, our simulations implied that to remain in the staggered configuration external forces need to be applied on the graphene layers, making the system difficult to realize in practice.

Interlayer sliding patterns under bending

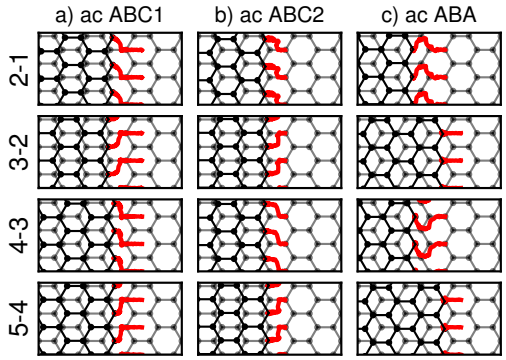

Figure 3.11: Relative sliding paths of individual graphene layers within the multilayer graphene stack. The numbers on the left are the layer numbers and they start from the top of the peeled stack. The followed atoms (red) are chosen close to the end of the peeled part of the stack and the atoms to the right from the followed ones are not shown for clarity. Interlayer slides in the ac-direction require shifts perpendicular to the ac-direction in order to avoid AA-stacking. The initial stacking affects how far the layer slides before the perpendicular shift in order to avoid AA-stacking is required. a) The ABC1 stacking allows long slide from AB -to BA-stacking before the AA-stacking is encountered and the layers need to shift in the $\hat{y}$-direction. b) ABC2 is initially BA-stacked and the AA-stacking barrier follows almost immediately after the sliding begins. Shifts in $\hat{y}$-direction are thus required already at early stages. c) For ABA-stacking every other layer pair encounters AA-stacking already at the beginning of the bending while every other pair only slides from AB -to BA stacking over the low saddle point in the corrugation potential. This gives layer shift patterns where layer pairs shift together.

In previous section we only considered bends with the optimal deflection angles ϕ_r where registry was obtained on both sides of the bend. For other bend angles the layers could not obtain good registry unless they also slid perpendicular ($\hat{y}$-direction, see

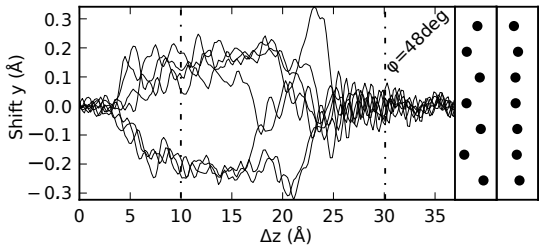

Figure 3.12: Average shift in perpendicular direction ($\hat{y}$) of each layer during the simulation. At pulling distance of $\Delta z = 30$ Å to the bend angle $\phi_r = 48°$, corresponding to slide from BA -to AB-stacking, is reached and the perpendicular shifts have vanished. The insets at right edge show snapshots of the layer shifts as viewed from the peeled end. The points of the layer shifts in the inset are marked by dashed lines in the main figure.

Fig. 3.8) to the peeling direction. The slides in the peeling direction, described in the previous section, were due to the layers avoiding in-plane deformations whereas sliding in the $\hat{y}$-direction at the peeled part, while remaining fixed at the bulk part, required shear in the bend region and thus increased the in-plane elastic energy. However, due to these $\hat{y}$-direction slides better registry was achieved for the peeled part which consequently decreased corrugation energy. The interplay between shear and registry effects was complex and only qualitative description of their relation could be given in the example cases.

We called the $\hat{y}$-direction layer movements at the peeled end as sliding patterns. These sliding patterns were studied by considering the projected paths of chosen atoms relative to the layers below (Fig. 3.11). For peeling in ac-direction all of the studied sliding paths implied avoidance of the AA-stacking by slides in $\hat{y}$-direction (Fig. 3.11). By other methods we showed that these $\hat{y}$-slides were enabled, as expected, by in-plane shear at the bend region. These sliding patterns were not as pronounced when the peeling was in the zz-direction since the optimal layer sliding path in the zz-direction does not require large shifts perpendicular to the sliding direction (Fig. 3.7a). Similar staggered sliding paths with stick and slip behavior have been observed in simulations pulling graphene flakes on graphene,[87] here we showed that these paths were also present in more constrained environment where these staggered paths required additional in-plane shear.

The sliding patterns were also studied by recording the average shift of each layer in the $\hat{y}$-direction as a function of the pulling distance Δz. The resulting curves showed the sliding patterns with individual fingerprint for each initial stacking and peeling direction. For example, when peeling ABC-stacked system initially BA-stacked in ac-direction, reaching AB-stacking required $2b$ slide in $-\hat{x}$-direction passing over low adhesion energy of the AA-stacking. The AA-stacking could be avoided only by shear in $\hat{y}$-direction, which was observed almost immediately after the peeling begun. However, after reaching optimal bend angle $\phi_r \approx 48°$, corresponding to slide of $2b$, at

pulling distance of $\Delta z = 30$ Å, the $\hat{y}$-shifts had almost completely vanished (Fig. 3.12) suggesting good registry without any $\hat{y}$-shift. The behavior was understood by the corrugation potential in picture (Fig. 3.7a) which suggests exactly this type of behavior for the layer slides in $-\hat{x}$-direction due to AA-stacking barrier between BA- and AB-stackings.

Here we only considered situations where the peeling was in some high symmetry direction of the graphene layers and the initial stacking of the systems were well-defined. In practice such well-defined structures and well controlled peeling is probably difficult to achieve. However, our finding that multilayer graphene should not remain in kinked configuration just by to the registry effects should be feasible to confirm by experiments. Already the lack of observations of kinked multilayer graphene should serve as a sanity check for of the simulation.

4 Summary & Outlook

In this thesis, studies on the mechanical and electromechanical properties of graphene systems have been presented. The elastic properties were studied by molecular dynamics simulations using classical force fields, density-functional tight-binding, and continuum sheet elasticity. In selected cases the density-functional tight-binding method was used to study the elastic deformations and relate the observed deformations with the changes in the electronic properties.

Revision of the Bloch's theorem, the revised periodic boundary conditions, enabled some novel approaches used in this thesis. Using the wedge symmetry we studied the temperature dependence on the bending rigidity of two-dimensional gold surface embedded in graphene, suggested in our article [V], and showed that it increases slightly with the temperature. The study of topological effects, namely Möbius topology, without deforming the graphene nanoribbon was made in our article [I]. We presented not only a unique method of studying topology, but also showed that the topological effects were short-ranged for the topological Möbius graphene nanoribbons. Using the revised periodic boundary conditions also the description of large graphene spirals became feasible in our article [II]. Using the minimal unit cell and chiral symmetry we probed the density of states changes near the equilibrium pitch and showed that the interlayer interactions are responsible for the electronic property changes in small elongations and the strain effects start to contribute only at very large elongations. Using classical force fields the spirals were shown to unfold by local peeling when external force was used to elongate the spiral. Recently, graphene spiral structures, with variable radius, have been fabricated experimentally.[62]

Classical force field simulations were used to describe large systems. Implementation of the registry dependent interlayer potential [15] enabled accurate simulations of two interesting setups. In our article [IV] we explained experimentally observed pinning phenomena, where graphene nanoribbons could be kept in bent configurations even without any visible impurities, only by lateral energy corrugations related to the registry. Additionally in our article [III] we showed that the lateral energy corrugations are not likely to be sufficient to maintain multilayer graphene stacks in a kinked configuration after external forces are released. We also observed intricate layer sliding patterns when bending multilayer graphene stacks. Again these patterns were explained by the registry effects between graphene layers.

In our article [IV] we studied the stability limits when graphene nanoribbons were by

external means bent on a substrate. During this bending, the inner edge of the ribbon became under compression. When a width dependent critical curvature was reached a large part of the ribbon buckled abruptly out of the substrate plane and the ribbon relaxed into a configuration with two straight parts connected by a buckled region.

Despite its very recent discovery graphene has already attracted huge amount of interest and it will probably continue to do so for several years. The amount of possible applications is vast and most likely not yet even fully understood. Graphene might be used in future electronics as well as in applications requiring extreme strength. However, particularly interesting applications can arise when the interplay between the electronic and mechanical properties is exploited via strain engineering. This thesis gives glimpses to the mechanical response of graphene under various stresses. In some cases the results explain experimentally observed behavior, as in article [IV], and in others present novel structures for experimental study, as in article [II]. Already today, the elastic behavior is important when considering the fabrication of graphene nanostructures but in future its importance might increase because of the possible control over the electronic structure. Even if our studies focused less on the electronic structure the mechanics results can be combined with other studies to obtain limits for the changes in the electronic structure, for example in a manner similar to our article [IV].

References

[1] International technology roadmap for semiconductors. `http://www.itrs2.net`. Accessed: 2016-05-15.

[2] K. S. Novoselov, A. K. Geim, S. V. Morozov, D. Jiang, Y. Zhang, S. V. Dubonos, I. V. Grigorieva, and A. A. Firsov. Electric field effect in atomically thin carbon films. *Science*, 306(5696):666–669, 2004.

[3] N.-C. Yeh, C.-C. Hsu, M. L. Teague, J.-Q. Wang, D. A. Boyd, and C.-C. Chen. Nanoscale strain engineering of graphene and graphene-based devices. *Acta Mechanica Sinica*, pages 1–13, 2016.

[4] Vitor M. Pereira and A. H. Castro Neto. Strain engineering of graphene's electronic structure. *Phys. Rev. Lett.*, 103:046801, Jul 2009.

[5] Changgu Lee, Xiaoding Wei, Jeffrey W. Kysar, and James Hone. Measurement of the elastic properties and intrinsic strength of monolayer graphene. *Science*, 321(5887):385–388, 2008.

[6] Yujie Wei, Baoling Wang, Jiangtao Wu, Ronggui Yang, and Martin L. Dunn. Bending rigidity and gaussian bending stiffness of single-layered graphene. *Nano Letters*, 13(1):26–30, 2013. PMID: 23214980.

[7] P. W. Atkins and R.S. Friedman. *Molecular quantum mechanics*. Oxford university press, Oxford, 3th edition, 1997.

[8] P. Hohenberg and W. Kohn. Inhomogeneous electron gas. *Phys. Rev.*, 136:B864–B871, Nov 1964.

[9] W. Kohn and L. J. Sham. Self-consistent equations including exchange and correlation effects. *Phys. Rev.*, 140:A1133–A1138, Nov 1965.

[10] Pekka Koskinen and Ville Makinen. Density-functional tight-binding for beginners. *Computational Materials Science*, 47(1):237 – 253, 2009.

[11] Donald W. Brenner. Empirical potential for hydrocarbons for use in simulating the chemical vapor deposition of diamond films. *Phys. Rev. B*, 42:9458–9471, Nov 1990.

[12] G. C. Abell. Empirical chemical pseudopotential theory of molecular and metallic bonding. *Phys. Rev. B*, 31:6184–6196, May 1985.

[13] J. Tersoff. Empirical interatomic potential for carbon, with applications to amorphous carbon. *Phys. Rev. Lett.*, 61:2879–2882, Dec 1988.

[14] J. E. Jones. On the determination of molecular fields. ii. from the equation of state of a gas. *Proceedings of the Royal Society of London A: Mathematical, Physical and Engineering Sciences*, 106(738):463–477, 1924.

[15] Aleksey N. Kolmogorov and Vincent H. Crespi. Registry-dependent interlayer potential for graphitic systems. *Phys. Rev. B*, 71:235415, Jun 2005.

[16] Steven J. Stuart, Alan B. Tutein, and Judith A. Harrison. A reactive potential for hydrocarbons with intermolecular interactions. *The Journal of Chemical Physics*, 112(14):6472–6486, 2000.

[17] Felix Bloch. Über die quantenmechanik der elektronen in kristallgittern. *Zeitschrift für Physik*, 52(7):555–600, 1929.

[18] Pekka Koskinen and Oleg O. Kit. Efficient approach for simulating distorted materials. *Phys. Rev. Lett.*, 105:106401, Aug 2010.

[19] Oleg O. Kit, Lars Pastewka, and Pekka Koskinen. Revised periodic boundary conditions: Fundamentals, electrostatics, and the tight-binding approximation. *Phys. Rev. B*, 84:155431, Oct 2011.

[20] Philip Wolfe. Convergence conditions for ascent methods. *SIAM Review*, 11(2):226–235, 1969.

[21] Philip Wolfe. Convergence conditions for ascent methods. ii: Some corrections. *SIAM Review*, 13(2):185–188, 1971.

[22] J. Nocedal and S. J. Wright. *Numerical Optimization*. Springer, New York, 2nd edition, 2006.

[23] Mark H. Holmes. *Introduction to Numerical Methods in Differential Equations*. Springer, 2006.

[24] T. Schneider and E. Stoll. Molecular-dynamics study of a three-dimensional one-component model for distortive phase transitions. *Phys. Rev. B*, 17:1302–1322, Feb 1978.

[25] L.D. Landau and E.M. Lifshitz. *Theory of elasticity*. Pergamon, Oxford, 3th edition, 1986.

[26] M.P. do Carmo. *Differential geometry of curves and surfaces*. Prentice-Hall, New Jersey, 1st edition, 1976.

[27] A. H. Castro Neto, F. Guinea, N. M. R. Peres, K. S. Novoselov, and A. K. Geim. The electronic properties of graphene. *Rev. Mod. Phys.*, 81:109–162, Jan 2009.

[28] P. R. Wallace. The band theory of graphite. *Phys. Rev.*, 71:622–634, May 1947.

[29] K. S. Novoselov, A. K. Geim, S. V. Morozov, D. Jiang, M. I. Katsnelson, I. V. Grigorieva, S. V. Dubonos, and A. A. Firsov. Two-dimensional gas of massless dirac fermions in graphene. *Nature*, 438(7065):197–200, Nov 2005.

[30] K. S. Novoselov, D. Jiang, F. Schedin, T. J. Booth, V. V. Khotkevich, S. V. Morozov, and A. K. Geim. Two-dimensional atomic crystals. *Proceedings of the National Academy of Sciences of the United States of America*, 102(30):10451–10453, 2005.

[31] Richard Balog, Bjarke Jorgensen, Louis Nilsson, Mie Andersen, Emile Rienks, Marco Bianchi, Mattia Fanetti, Erik Laegsgaard, Alessandro Baraldi, Silvano Lizzit, Zeljko Sljivancanin, Flemming Besenbacher, Bjork Hammer, Thomas G. Pedersen, Philip Hofmann, and Liv Hornekaer. Bandgap opening in graphene induced by patterned hydrogen adsorption. *Nat Mater*, 9(4):315–319, Apr 2010.

[32] Melinda Y. Han, Barbaros Özyilmaz, Yuanbo Zhang, and Philip Kim. Energy band-gap engineering of graphene nanoribbons. *Phys. Rev. Lett.*, 98:206805, May 2007.

[33] Young-Woo Son, Marvin L. Cohen, and Steven G. Louie. Energy gaps in graphene nanoribbons. *Phys. Rev. Lett.*, 97:216803, Nov 2006.

[34] Vitor M. Pereira, A. H. Castro Neto, and N. M. R. Peres. Tight-binding approach to uniaxial strain in graphene. *Phys. Rev. B*, 80:045401, Jul 2009.

[35] Giulio Cocco, Emiliano Cadelano, and Luciano Colombo. Gap opening in graphene by shear strain. *Phys. Rev. B*, 81:241412, Jun 2010.

[36] Zhen Hua Ni, Ting Yu, Yun Hao Lu, Ying Ying Wang, Yuan Ping Feng, and Ze Xiang Shen. Uniaxial strain on graphene: Raman spectroscopy study and band-gap opening. *ACS Nano*, 2(11):2301–2305, 2008. PMID: 19206396.

[37] M. Farjam and H. Rafii-Tabar. Comment on "band structure engineering of graphene by strain: First-principles calculations". *Phys. Rev. B*, 80:167401, Oct 2009.

[38] I. I. Naumov and A. M. Bratkovsky. Gap opening in graphene by simple periodic inhomogeneous strain. *Phys. Rev. B*, 84:245444, Dec 2011.

[39] Pekka Koskinen, Sami Malola, and Hannu Häkkinen. Self-passivating edge reconstructions of graphene. *Phys. Rev. Lett.*, 101:115502, Sep 2008.

[40] Pekka Koskinen, Sami Malola, and Hannu Häkkinen. Evidence for graphene edges beyond zigzag and armchair. *Phys. Rev. B*, 80:073401, Aug 2009.

[41] Kazu Suenaga and Masanori Koshino. Atom-by-atom spectroscopy at graphene edge. *Nature*, 468(7327):1088–1090, Dec 2010.

[42] Yang Lu and Jing Guo. Band gap of strained graphene nanoribbons. *Nano Research*, 3(3):189–199, 2010.

[43] Fei Ma, Zhankui Guo, Kewei Xu, and Paul K. Chu. First-principle study of energy band structure of armchair graphene nanoribbons. *Solid State Communications*, 152(13):1089 – 1093, 2012.

[44] Xihong Peng and Selina Velasquez. Strain modulated band gap of edge passivated armchair graphene nanoribbons. *Applied Physics Letters*, 98(2), 2011.

[45] Yang Lu and Jing Guo. Band gap of strained graphene nanoribbons. *Nano Research*, 3(3):189–199, 2010.

[46] D.-B. Zhang, E. Akatyeva, and T. Dumitrică. Bending ultrathin graphene at the margins of continuum mechanics. *Phys. Rev. Lett.*, 106:255503, Jun 2011.

[47] Juan Atalaya, Andreas Isacsson, and Jari M. Kinaret. Continuum elastic modeling of graphene resonators. *Nano Letters*, 8(12):4196–4200, 2008. PMID: 18956921.

[48] Y. Huang, J. Wu, and K. C. Hwang. Thickness of graphene and single-wall carbon nanotubes. *Phys. Rev. B*, 74:245413, Dec 2006.

[49] V. B. Shenoy, C. D. Reddy, A. Ramasubramaniam, and Y. W. Zhang. Edge-stress-induced warping of graphene sheets and nanoribbons. *Phys. Rev. Lett.*, 101:245501, Dec 2008.

[50] C D Reddy, Yong-Wei Zhang, and V B Shenoy. Influence of substrate on edge rippling in graphene sheets. *Modelling and Simulation in Materials Science and Engineering*, 19(5):054007, 2011.

[51] Niklas Lindahl, Daniel Midtvedt, Johannes Svensson, Oleg A. Nerushev, Niclas Lindvall, Andreas Isacsson, and Eleanor E. B. Campbell. Determination of the bending rigidity of graphene via electrostatic actuation of buckled membranes. *Nano Letters*, 12(7):3526–3531, 2012. PMID: 22708530.

[52] Emiliano Cadelano, Stefano Giordano, and Luciano Colombo. Interplay between bending and stretching in carbon nanoribbons. *Phys. Rev. B*, 81:144105, Apr 2010.

[53] The international space elevator consortium. `http://www.isec.org`. Accessed: 2016-05-10.

[54] Qiang Lu, Marino Arroyo, and Rui Huang. Elastic bending modulus of monolayer graphene. *Journal of Physics D: Applied Physics*, 42(10):102002, 2009.

[55] Balazs Hajgato, Songül Güryel, Yves Dauphin, Jean-Marie Blairon, Hans E. Miltner, Gregory Van Lier, Frank De Proft, and Paul Geerlings. Theoretical investigation of the intrinsic mechanical properties of single- and double-layer graphene. *The Journal of Physical Chemistry C*, 116(42):22608–22618, 2012.

[56] I. Nikiforov, E. Dontsova, R. D. James, and T. Dumitrică. Tight-binding theory of graphene bending. *Phys. Rev. B*, 89:155437, Apr 2014.

[57] Pekka Koskinen and Oleg O. Kit. Approximate modeling of spherical membranes. *Phys. Rev. B*, 82:235420, Dec 2010.

[58] R. Nicklow, N. Wakabayashi, and H. G. Smith. Lattice dynamics of pyrolytic graphite. *Phys. Rev. B*, 5:4951–4962, Jun 1972.

[59] U. Monteverde, J. Pal, M.A. Migliorato, M. Missous, U. Bangert, R. Zan, R. Kashtiban, and D. Powell. Under pressure: Control of strain, phonons and bandgap opening in rippled graphene. *Carbon*, 91:266 – 274, 2015.

[60] Kuan Zhang and Marino Arroyo. Understanding and strain-engineering wrinkle networks in supported graphene through simulations. *Journal of the Mechanics and Physics of Solids*, 72:61 – 74, 2014.

[61] Alex Smolyanitsky. Molecular dynamics simulation of thermal ripples in graphene with bond-order-informed harmonic constraints. *Nanotechnology*, 25(48):485701, 2014.

[62] Melina K. Blees, Arthur W. Barnard, Peter A. Rose, Samantha P. Roberts, Kathryn L. McGill, Pinshane Y. Huang, Alexander R. Ruyack, Joshua W. Kevek, Bryce Kobrin, David A. Muller, and Paul L. McEuen. Graphene kirigami. *Nature*, 524(7564):204–207, Aug 2015. Letter.

[63] A. Fasolino, J. H. Los, and M. I. Katsnelson. Intrinsic ripples in graphene. *Nat Mater*, 6(11):858–861, Nov 2007.

[64] P. Liu and Y. W. Zhang. Temperature-dependent bending rigidity of graphene. *Applied Physics Letters*, 94(23), 2009.

[65] K. V. Zakharchenko, J. H. Los, M. I. Katsnelson, and A. Fasolino. Atomistic simulations of structural and thermodynamic properties of bilayer graphene. *Phys. Rev. B*, 81:235439, Jun 2010.

[66] Philipp Wagner, Christopher P. Ewels, Viktoria V. Ivanovskaya, Patrick R. Briddon, Amand Pateau, and Bernard Humbert. Ripple edge engineering of graphene nanoribbons. *Phys. Rev. B*, 84:134110, Oct 2011.

[67] C. D. Reddy, A. Ramasubramaniam, V. B. Shenoy, and Yong-Wei Zhang. Edge elastic properties of defect-free single-layer graphene sheets. *Applied Physics Letters*, 94(10), 2009.

[68] N. W. Ashcroft and N. D. Mermin. *Solid State Physics*. Holt, Rinehart, and Winston, New York, 1st edition, 1976.

[69] Rohith P. John, Mira Park, Dohyun Moon, Kyungjin Lee, Seunghee Hong, Yang Zou, Chang Seop Hong, and Myoung Soo Lah. A chiral pentadecanuclear metallamacrocycle with a sextuple twisted möbius topology. *Journal of the American Chemical Society*, 129(46):14142–14143, 2007. PMID: 17960933.

[70] D. Ajami, O. Oeckler, A. Simon, and R. Herges. Synthesis of a mobius aromatic hydrocarbon. *Nature*, 426(6968):819–821, Dec 2003.

[71] Xianlong Wang, Xiaohong Zheng, Meiyan Ni, Liangjian Zou, and Zhi Zeng. Theoretical investigation of mobius strips formed from graphene. *Applied Physics Letters*, 97(12), 2010.

[72] E. L. Starostin and G. H. M. van der Heijden. The shape of a mobius strip. *Nat Mater*, 6(8):563–567, Aug 2007.

[73] T. A. Witten. Stress focusing in elastic sheets. *Rev. Mod. Phys.*, 79:643–675, Apr 2007.

[74] David J. Wales* and Jonathan P. K. Doye. Global optimization by basin-hopping and the lowest energy structures of lennard-jones clusters containing up to 110 atoms. *The Journal of Physical Chemistry A*, 101(28):5111–5116, 1997.

[75] Joost van der Lit, Peter H Jacobse, Daniel Vanmaekelbergh, and Ingmar Swart. Bending and buckling of narrow armchair graphene nanoribbons via stm manipulation. *New Journal of Physics*, 17(5):053013, 2015.

[76] Xiaofeng Feng, Sangku Kwon, Jeong Young Park, and Miquel Salmeron. Superlubric sliding of graphene nanoflakes on graphene. *ACS Nano*, 7(2):1718–1724, 2013. PMID: 23327483.

[77] Yilun Liu, François Grey, and Quanshui Zheng. The high-speed sliding friction of graphene and novel routes to persistent superlubricity. *Scientific Reports*, 4:4875 EP –, May 2014. Article.

[78] Shigeki Kawai, Andrea Benassi, Enrico Gnecco, Hajo Söde, Rémy Pawlak, Xinliang Feng, Klaus Müllen, Daniele Passerone, Carlo A. Pignedoli, Pascal Ruffieux, Roman Fasel, and Ernst Meyer. Superlubricity of graphene nanoribbons on gold surfaces. *Science*, 351(6276):957–961, 2016.

[79] Otakar Frank, Georgia Tsoukleri, John Parthenios, Konstantinos Papagelis, Ibtsam Riaz, Rashid Jalil, Kostya S. Novoselov, and Costas Galiotis. Compression behavior of single-layer graphenes. *ACS Nano*, 4(6):3131–3138, Jun 2010.

[80] Charalampos Androulidakis, Emmanuel N. Koukaras, Otakar Frank, Georgia Tsoukleri, Dimitris Sfyris, John Parthenios, Nicola Pugno, Konstantinos Papagelis, Kostya S. Novoselov, and Costas Galiotis. Failure processes in embedded monolayer graphene under axial compression. *Scientific Reports*, 4:5271 EP –, Jun 2014. Article.

[81] Yuanwen Gao and Peng Hao. Mechanical properties of monolayer graphene under tensile and compressive loading. *Physica E: Low-dimensional Systems and Nanostructures*, 41(8):1561 – 1566, 2009.

[82] M. Neek-Amal and F. M. Peeters. Graphene nanoribbons subjected to axial stress. *Phys. Rev. B*, 82:085432, Aug 2010.

[83] Kuijian Yang, Yuli Chen, Fei Pan, Shengtao Wang, Yong Ma, and Qijun Liu. Buckling behavior of substrate supported graphene sheets. *Materials*, 9(1):32, 2016.

[84] Duoming Wang, Guorui Chen, Chaokai Li, Meng Cheng, Wei Yang, Shuang Wu, Guibai Xie, Jing Zhang, Jing Zhao, Xiaobo Lu, Peng Chen, Guole Wang, Jianling Meng, Jian Tang, Rong Yang, Congli He, Donghua Liu, Dongxia Shi, Kenji Watanabe, Takashi Taniguchi, Ji Feng, Yuanbo Zhang, and Guangyu Zhang. Thermally induced graphene rotation on hexagonal boron nitride. *Phys. Rev. Lett.*, 116:126101, Mar 2016.

[85] P. Koskinen. Graphene nanoribbons subject to gentle bends. *Phys. Rev. B*, 85:205429, May 2012.

[86] Dai-Ming Tang, Dmitry G. Kvashnin, Sina Najmaei, Yoshio Bando, Koji Kimoto, Pekka Koskinen, Pulickel M. Ajayan, Boris I. Yakobson, Pavel B. Sorokin, Jun Lou, and Dmitri Golberg. Nanomechanical cleavage of molybdenum disulphide atomic layers. *Nat Commun*, 5, Apr 2014.

[87] M. M. van Wijk, M. Dienwiebel, J. W. M. Frenken, and A. Fasolino. Superlubric to stick-slip sliding of incommensurate graphene flakes on graphite. *Phys. Rev. B*, 88:235423, Dec 2013.